DOMINANT CONTROL ON RESERVOIR-FLOW BEHAVIOR IN CARBONATE RESERVOIRS AS DETERMINED FROM OUTCROP STUDIES*

R. K. Senger, F. J. Lucia, C. Kerans, and M. A. Ferris

Bureau of Economic Geology
The University of Texas at Austin
Austin, Texas 78713-7508

G. E. Fogg

Department of Land, Air, and Water Resources
University of California at Davis
Davis, California 95616

I. INTRODUCTION

The investigation of carbonate-ramp deposits of the upper San Andres Formation that crop out along the Algerita Escarpment, New Mexico, is a research element of ongoing geologic and petrophysical studies conducted at the Bureau of Economic Geology's Reservoir Characterization Research Laboratory (RCRL). The primary goal of the investigation is to develop an integrated strategy involving geological, petrophysical, geostatistical, and reservoir-simulation studies that can be used to better predict flow characteristics in analogous subsurface reservoirs. Geologic investigations and detailed measurements of petrophysical parameters on continuous outcrop were used to determine not only the vertical distribution of the data but also their lateral distribution, which is typically lacking in subsurface studies.

To characterize the complex heterogeneity associated with depositional and diagenetic processes at the interwell scale, detailed permeability data were collected within the overall geologic framework from the outcrop at Lawyer Canyon, Algerita Escarpment, New Mexico (fig. 1). Geologic mapping showed a series of upward-shallowing parasequences (10 to 40 ft thick and several thousand feet long). Parasequence boundaries are typically marked by tight mudstone/wackestone beds that display variable degrees of lateral continuity ranging from several hundred feet to more than 2,500 ft and are potentially important as flow barriers (fig. 2). Within these parasequences, distinct variability of facies and petrophysical characteristics is present at scales well below those of interwell spacing typical for their subsurface counterparts (660 to 1,330 ft). Pore types and permeability-porosity relationships can also be specific to individual parasequences.

*Publication authorized by the Director, Bureau of Economic Geology, The University of Texas at Austin.

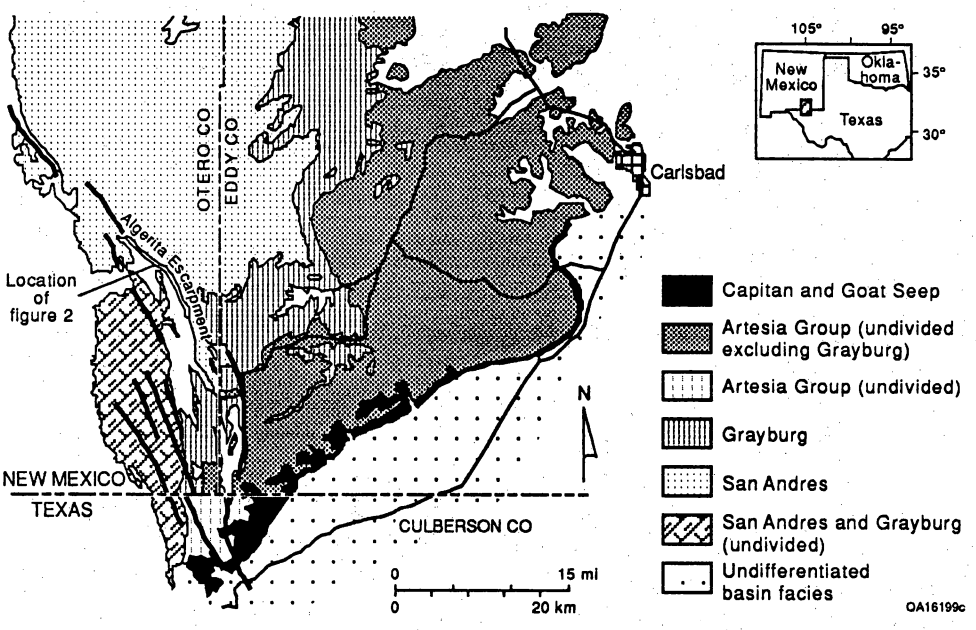

Figure 1. Geologic map of the Guadalupe Mountains compiled from Hayes (1964) and King (1948) showing the Algerita Escarpment and the Lawyer Canyon study area.

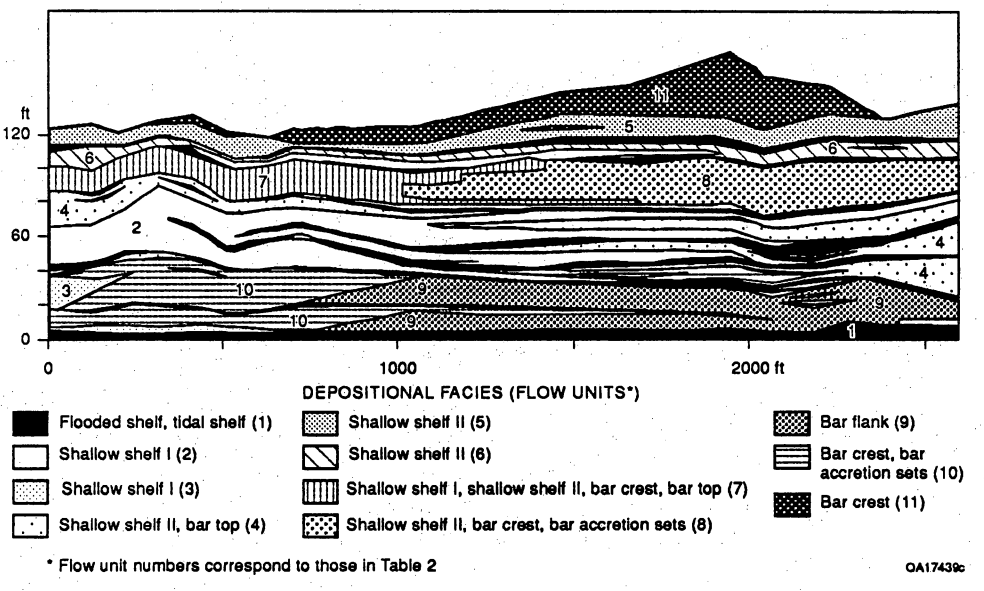

Figure 2. Distribution and geometry of depositional facies mapped in the upper San Andres parasequence window, Lawyer Canyon, Algerita Escarpment, New Mexico.

Previous studies characterizing permeability in San Andres outcrops include those of Hindrichs and others (1986) and Kittridge and others (1990). The study by Hindrichs and others was based on core plugs taken from different beds in the middle San Andres Formation. Results indicated large permeability variations within beds separated by low-permeability mudstones, with no apparent difference in permeability between horizontal and vertical cores. Kittridge and others (1990) used a mechanical field permeameter (MFP) to study spatial permeability variations at a specific site near the middle and upper San Andres Formation boundary at the Lawyer Canyon area. Geostatistical analyses of measured permeability indicated that permeability correlation lengths decreased with decreasing sample spacing and that different rock fabrics exhibited different mean permeabilities.

In this study, permeability measurements were guided by the detailed geologic mapping of continuous San Andres outcrop, which revealed a stacking pattern of parasequences and of facies and rock-fabric succession within parasequences that provide the necessary framework for petrophysical quantification of geologic models. Standard statistics were used to relate permeability to facies and rock-fabric characteristics through a petrophysical/rock-fabric approach. In addition, geostatistical analysis was applied to evaluate spatial permeability characteristics. Stochastic modeling was then used to generate a series of "realistic" permeability distributions that took into account the underlying permeability structure and the uncertainty of measurement data. Numerical waterflood simulations of selected permeability realizations were designed to characterize interwell heterogeneity and to represent heterogeneity by appropriate average properties, which can be used in reservoir-scale flow models. For the reservoir-scale flow model, a petrophysical/rock-fabric approach was used to quantify the geologic framework of the reservoir-flow model.

II. METHODOLOGY

A. Permeability Measurements

Permeability was measured with an MFP, which gauges gas-flow rates and pressure drop by pressing an injection tip against the rock surface. These data are used to calculate permeability values on the basis of a modified form of Darcy's law that incorporates effects of gas slippage at high velocity (Goggin and others, 1988). In addition, permeability and porosity were determined on the basis of conventional Hassler sleeve methods, using 1-inch-diameter core plugs taken from the outcrop. Core and MFP permeability compared reasonably well for permeabilities greater than about 1 md, which is approximately the detection limit of MFP measurements (Goggin and others, 1988).

The distribution of permeability measurements taken from the upper San Andres at Lawyer Canyon is shown in figure 3. Sampling focused on parasequence 1, composed of grainstones forming bar-crest and bar-flank facies overlying wackestones and mudstones of a flooded-shelf facies, and on parasequence 7, characterized by low-moldic and highly moldic grainstones (fig. 2). Permeability distributions were measured at scales ranging from detailed grids of 1-inch spacing to 1-ft spacing and at vertical transects that were spaced laterally between 5 and 100 ft and that contained permeability measurements at 1-ft vertical intervals.

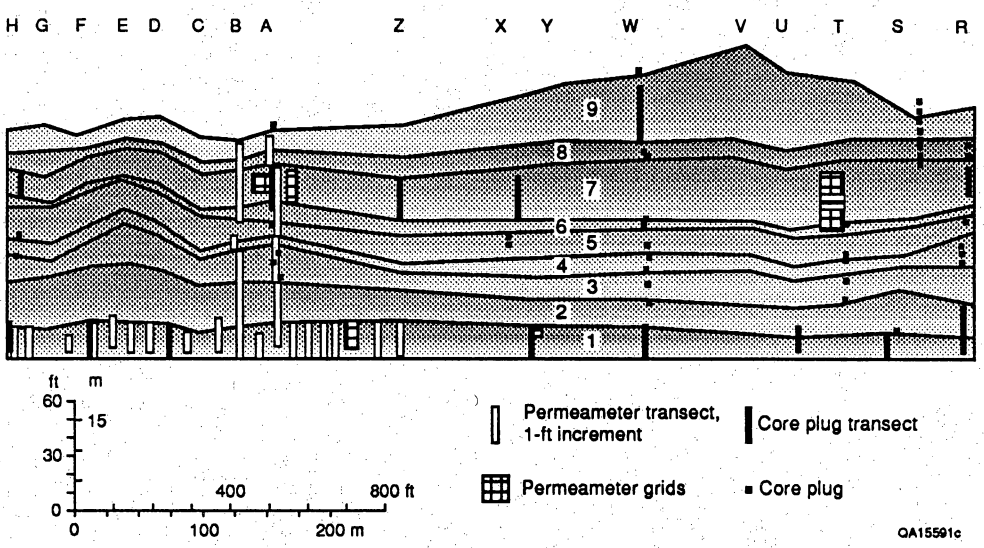

Figure 3. Location of sampling grids and transects of MFP measurements and core plugs.

The total number of MFP measurements at the Lawyer Canyon parasequence window was 1,584. Removing the outer weathering surface of the rock by chipping away an area of about 1 square inch gave the best representation of permeability (Ferris, in preparation). Preparing the sampling surface with a grinder produced permeabilities that were lower overall than those measured on chipped surfaces, owing to plugging of pore space by fines (Kittridge and others, 1990). Within each chipped area, typically several measurements were made and averaged. Depending on measurement discrepancies, as many as six different MFP readings were taken at various locations within the chipped area.

B. Geostatistics

Variography, a geostatistical technique for analyzing spatial variability of a property such as permeability, was used to help quantify the spatial permeability pattern at different scales. For further discussion of variogram analysis, refer to Journel and Huijbregts (1978) and Fogg and Lucia (1990). The variogram describes variability as a function of distance between measurements. The average variance of measurement pairs within certain distance intervals typically shows increasing variability (γ) with increasing interval range (fig. 4). Beyond a certain distance (range), γ may no longer increase. The variance that corresponds to the range is the sill, which reflects the variability where spatial correlation no longer exists; it typically corresponds to the ensemble variance of the entire data set. Small-scale heterogeneity or measurement errors can cause a variogram to originate at a high variance referred to as a nugget, representing local random variability.

Spatial permeability characteristics can often be described by the nugget, the correlation range, the sill, and the variogram model. The latter is obtained by fitting

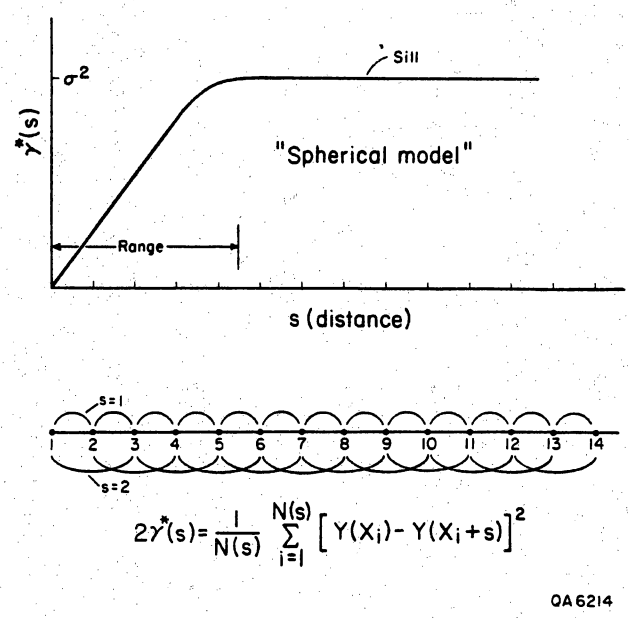

Figure 4. Schematic example of calculation of the experimental variogram.

a certain type of mathematical function to the experimental variogram. In this study the computer program GAMUK (Knudsen and Kim, 1978) was used to compute the experimental variogram. Application of the variogram to kriging or to conditional simulation usually requires an assumption of stationarity, which requires that the mean and the variogram be the same over the area of interest.

Kriging is a technique of estimating properties at points or blocks distributed over the area of interest by taking a weighted average of sample measurements surrounding a regularly spaced grid point or block. Kriging incorporates the spatial correlation structure contained in the variogram model. The kriging program is based on the program UKRIG, developed by Knudsen and Kim (1978). The permeability data were contoured with the CPS-1 contouring package (Radian Corp., 1989) and with the DI-3000 contouring package at The University of Texas Center for High Performance Computing.

Conditional simulation uses the underlying permeability structure obtained from kriging and adds the stochastic component associated with the uncertainty of the limited permeability data. Conditional simulation is performed with the program SIMPAN (Fogg, 1989). A large number of permeability realizations are screened for maximum and minimum continuity of permeable zones using the program MCSTAT (Fogg, 1989), which measures the length and thickness of domains of contiguous blocks having simulated permeability values greater than 50 md. The selection of realizations having low and high continuity of permeable zones is based on the mean horizontal continuity ($\overline{C_h}$) at the 10th and 90th percentiles, respectively. These end-member representations of "realistic" permeability distributions, conditioned on the same permeability data, are then used in waterflood simulations to evaluate

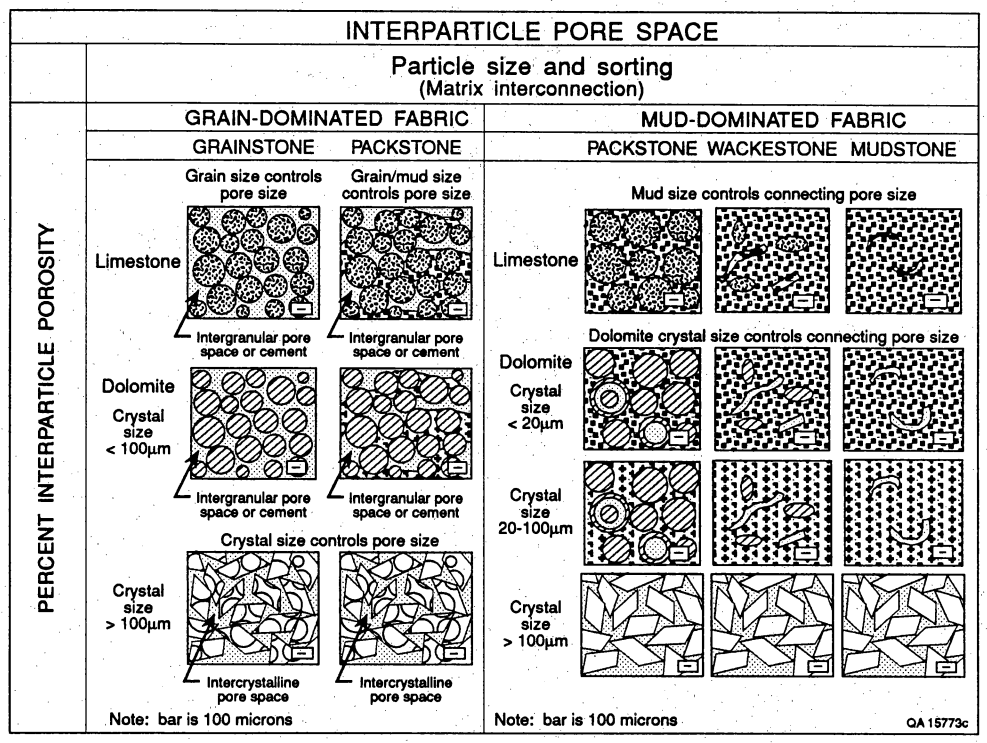

Figure 5. Classification of interparticle pore space in carbonate rocks.

reservoir-flow characteristics. For further details on stochastic reservoir simulations, refer to Fogg and others (1991). The reservoir simulator ECLIPSE (ECL Petroleum Technologies, 1990) was used in this study for two-phase waterflood simulations.

III. PERMEABILITY CHARACTERIZATION, LAWYER CANYON OUTCROP

A. Petrophysical/Rock-Fabric Approach

Petrophysical parameters such as porosity, permeability, and saturation were quantified by relating rock texture to pore-type and pore-size distribution (fig. 5). Spatial distribution of these petrophysical parameters was defined by geologic concepts of sedimentation, diagenesis, and tectonics, which provided the basis for the three-dimensional reservoir framework. Pore space in carbonate rocks can be divided into interparticle and vuggy pores on the basis of the particulate nature of carbonate rocks (Lucia, 1983). Three petrophysical/rock-fabric classes for nonvuggy pore space can be distinguished on the basis of porosity, permeability, and saturation relationships (fig. 6), and vuggy pore space can be divided into separate vugs (moldic, intrafossil, etc.) and touching vugs (cavernous, fractures, etc.) on the basis of the type of interconnection. The petrophysical classes for nonvuggy pores have distinct porosity-permeability relationships (fig. 7a), as well as relationships between porosity and water saturation (fig. 8).

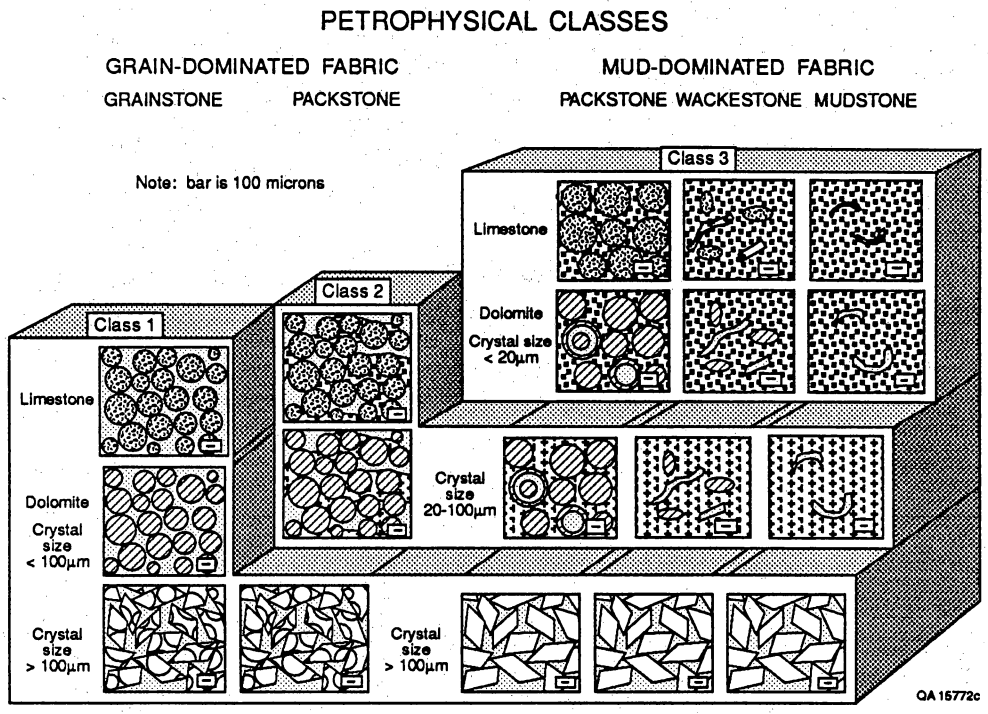

Figure 6. Petrophysical/rock-fabric classes for nonvuggy carbonates.

In addition to the nonvuggy pore types, separate vugs were important to this study. Separate vugs, such as moldic pores, are connected only through interparticle pore space and result in a lower permeability than that which would be expected if the porosity were all interparticle; that is, they do not fall into the different porosity-permeability field for nonvuggy pore types (fig. 7b). However, vuggy pore space is typically large enough that it can be assumed to be filled with hydrocarbons.

According to this rock-fabric classification, five productive rock-fabric units were recognized in the outcrop at the Lawyer Canyon parasequence window (fig. 9): grainstones, separate-vug grainstones, grain-dominated packstones, mud-dominated packstones and wackestones, and tight mudstones and fenestral caps. The information was derived from permeability and porosity measurements of core plugs and from a petrographic description of thin section taken from core plugs.

For the evaluation of permeability characteristics with respect to facies and fabrics, only those data were taken that follow the geologic measured sections for which spatial coordinates, facies, and fabric designations are available. The histogram of permeabilities using both core and MFP measurements (fig. 10) shows a roughly lognormal distribution. Core permeabilities are skewed toward lower permeabilities than are the MFP measurements, owing to the 1-md detection limit of the MFP data. Within relatively permeable facies (e.g., the bar-crest facies within parasequence 1), core and MFP measurements have statistically similar populations,

(a)

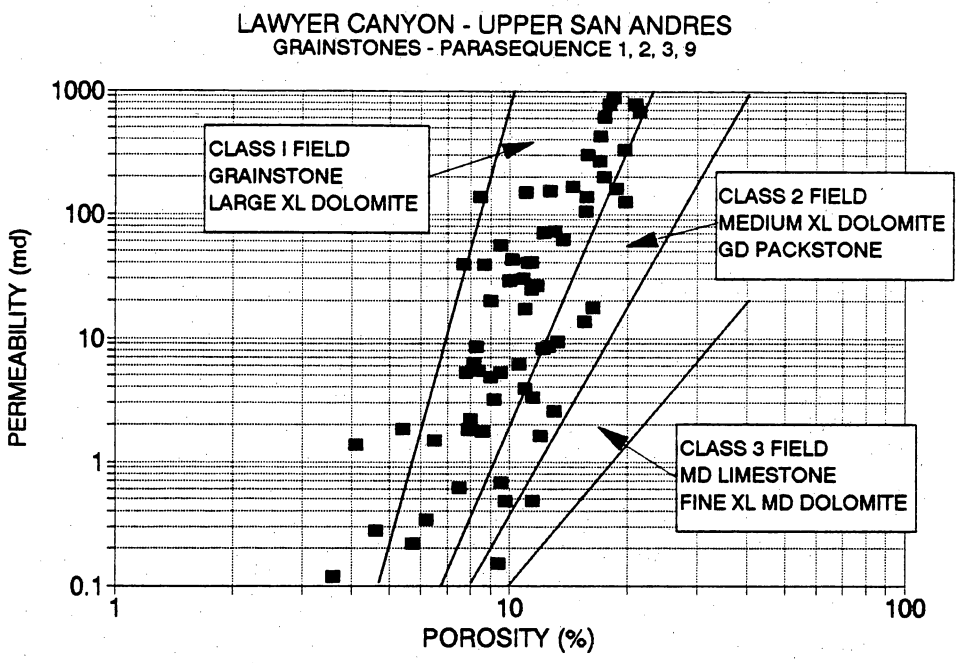

(b)

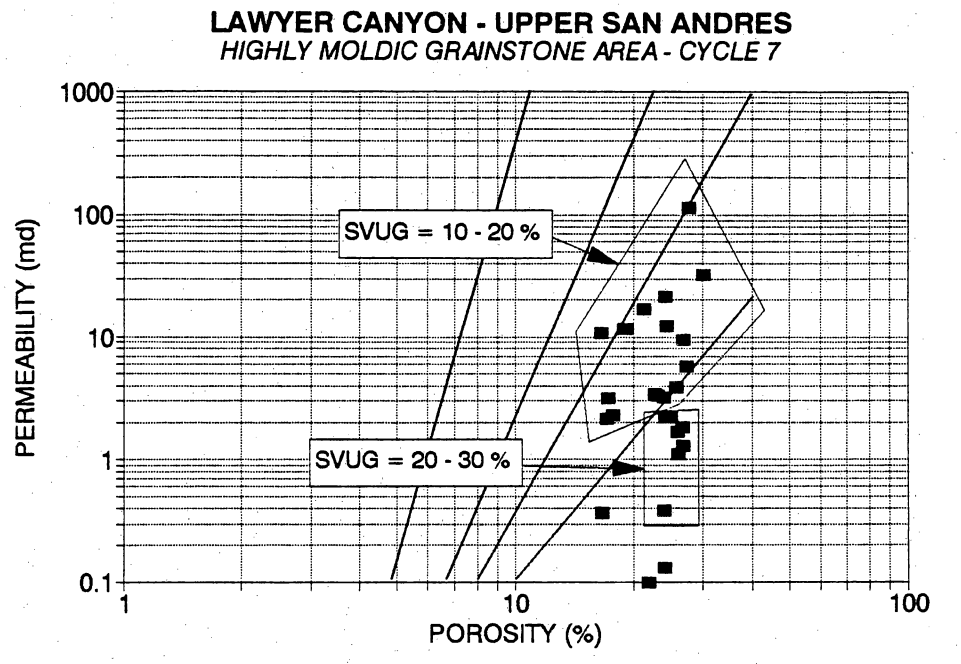

Figure 7. Porosity-permeability relationships for various rock-fabric fields in nonvuggy carbonates. Data are from core-plug measurements of (a) nonvuggy grainstones and (b) highly moldic grainstones from the Lawyer Canyon outcrop.

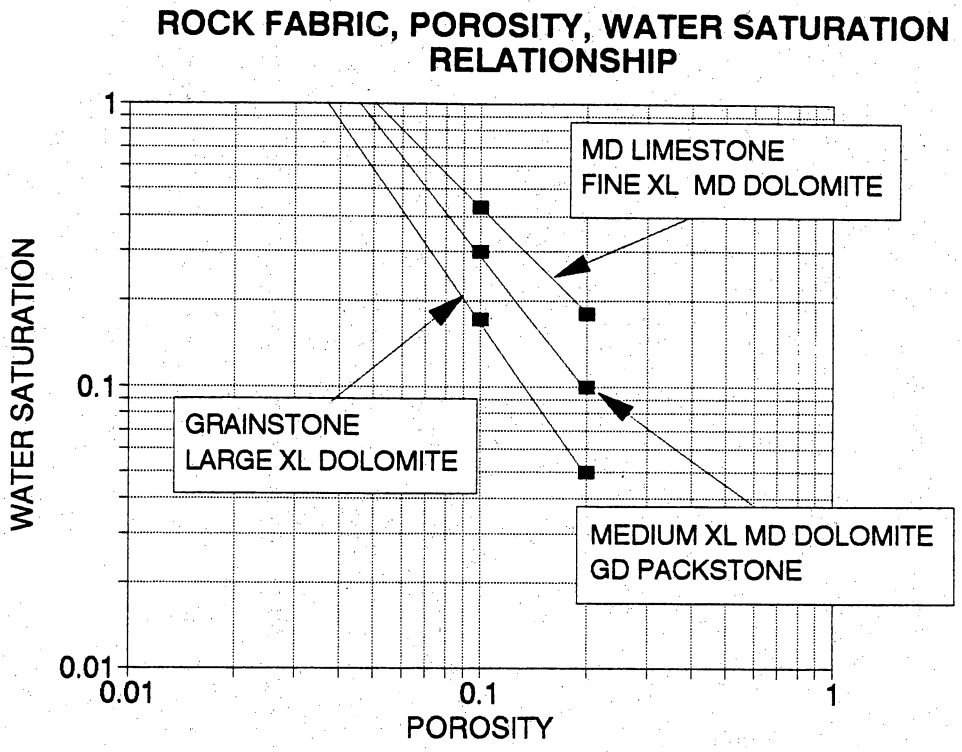

Figure 8. Rock-fabric, porosity, and water-saturation relationships from capillary-pressure curves.

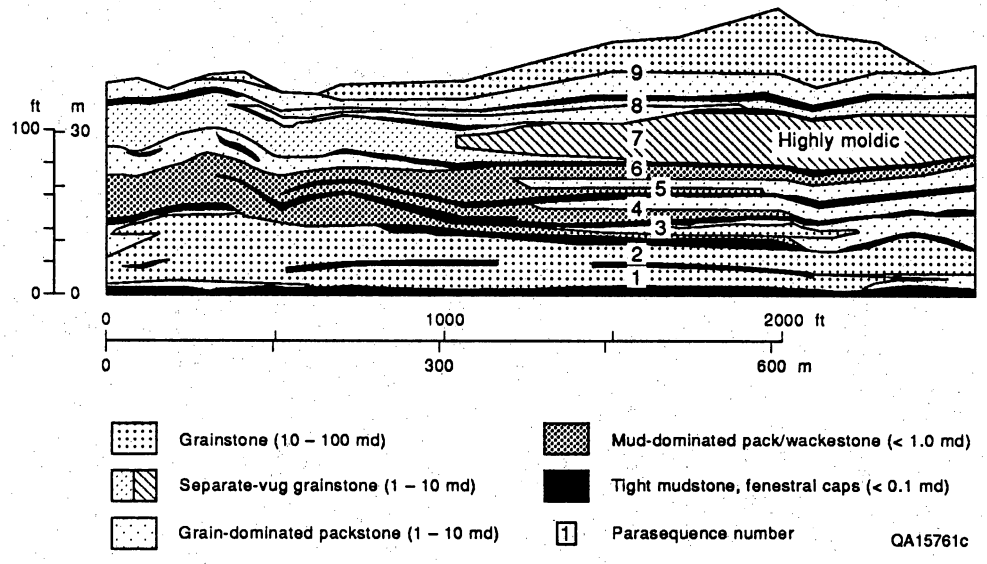

Figure 9. Rock-fabric flow units of the upper San Andres parasequence window, Lawyer Canyon, Algerita Escarpment, New Mexico.

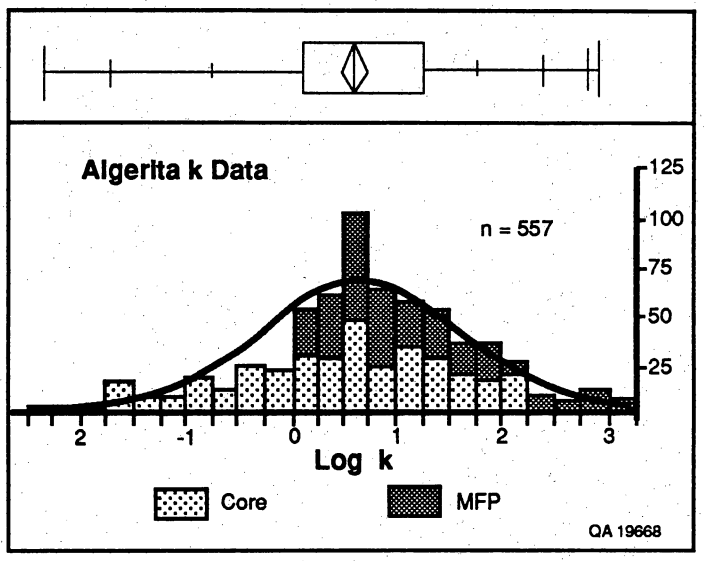

Figure 10. Histogram of permeabilities obtained along the geologically measured sections.

with similar geometric means of 1.33 and 1.34 md, respectively. Statistical comparison of the two populations using a t-test indicates that the null hypothesis cannot be rejected at the 80 percent confidence level (t-statistics = –0.1318; p-value = 0.8953).

The dominant rock fabrics exhibit significant differences in mean permeability (fig. 11), with mudstone having the lowest permeability and grainstone having the highest permeability. Most of the mapped facies are also characterized by significantly different mean permeabilities (fig. 12). Generally, shelf facies exhibit significantly lower mean permeabilities than bar facies, with the bar-crest and bar-accretion-set facies having the highest mean permeability of log k = 1.1 md. The facies characteristic (fig. 12) is consistent with the rock-fabric characteristic (fig. 11) because the bar facies consist mostly of high-permeability grainstones and the shelf facies consist mostly of low-permeability, mud-dominated fabrics. Furthermore, the mapped parasequences are characterized by different facies and fabric combinations, indicating different hydraulic properties of each parasequence. Mean permeabilities in parasequences 1, 2, 7, and 9 are significantly higher than those in parasequences 3, 4, 5, 6, and 8. The latter sequences consist mostly of packstone and wackestone, whereas parasequences 1, 2, 7, and 9 consist predominantly of grainstones (fig. 9). Grainstones in parasequence 7 are characterized by moldic-pore types with high porosity but slightly lower permeability than those in the other cycles having intergranular porosity.

Within individual facies, permeability varies by as much as five orders of magnitude (fig. 12). Characterization of spatial permeability patterns within individual facies is therefore important for predicting flow behavior in these ramp-crest grainstone bar complexes. If permeability within facies is spatially uncorrelated (i.e., random), then the two-dimensional effective permeability of that facies can be

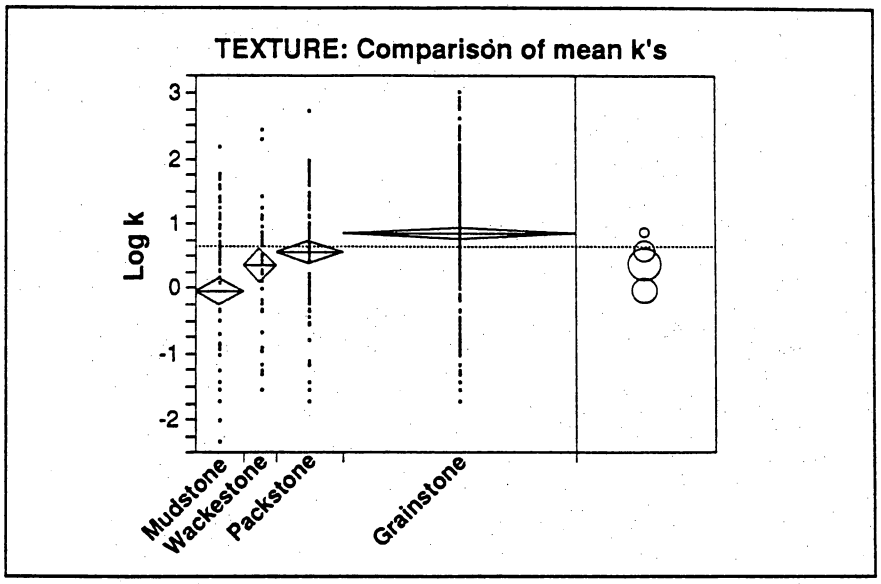

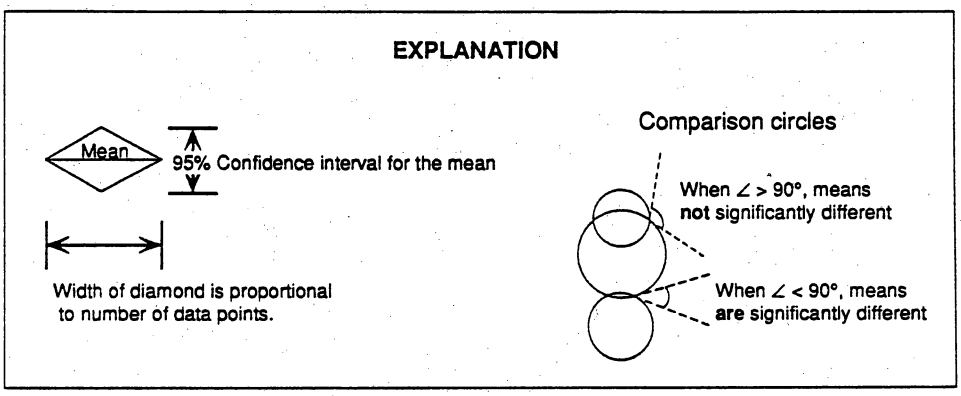

Figure 11. Statistical comparison of means of permeability for different textures. Comparison circles correspond to the 95 percent confidence intervals for the means.

estimated by taking the geometric average of the local permeabilities (Warren and Price, 1961). If permeability within facies exhibits significant spatial correlation, then effective permeability of that facies must be estimated by taking some other type of average.

B. Spatial Permeability Patterns and Variography

Spatial patterns in permeability were characterized and mapped in three steps. First, the data were contoured with an inverse-distance-squared algorithm to depict any trends or anisotropies in the data. Second, variograms were computed for

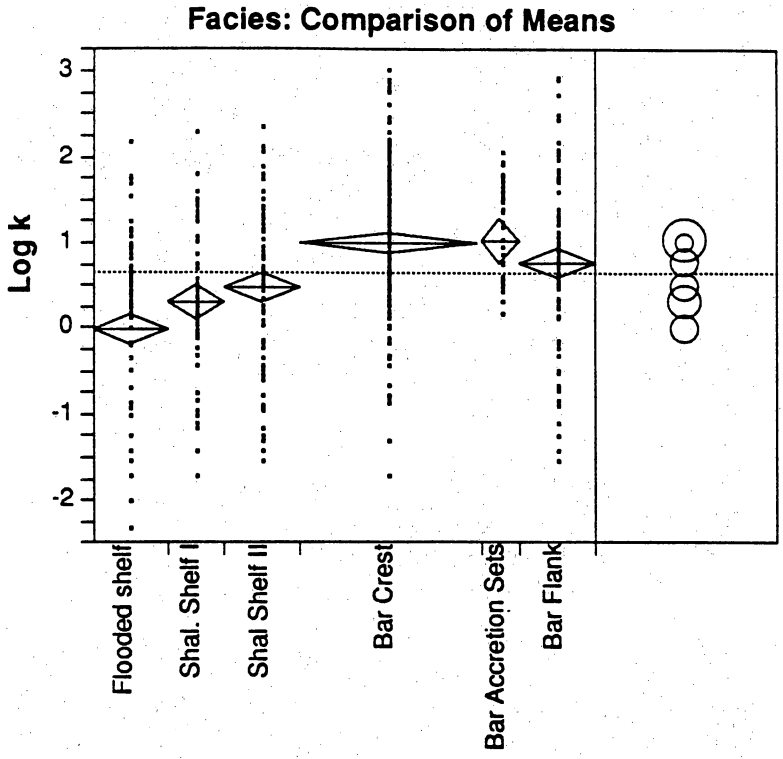

Mean Estimates

Facies	N	Mean	Std Error
Flooded shelf	82	-0.01	0.10
Shallow shelf I	48	0.25	0.13
Shallow shelf II	73	0.51	0.11
Bar crest	158	1.07	0.07
Bar top	6	0.10	0.37
Tidal flat	2	0.37	0.65
Bar accretion sets	18	1.11	0.22
Bar flank	82	0.76	0.10
Shallow shelf I (moldic)	16	0.45	0.23
Shallow shelf II (moldic)	9	0.26	0.30
Bar crest (moldic)	39	0.73	0.15
Bar accretion sets (moldic)	24	0.98	0.19

Figure 12. Statistical comparison of means of permeability for different facies. Standard error values refer to the estimated means.

different lag spacings and directions that were consistent with the data spacings and inverse-distance maps. Third, variogram models were fit to the variograms and were used to create point-kriged maps of spatial permeability patterns.

Standard contouring (inverse-distance-squared) of the detailed permeability transects spaced between 25 and 100 ft in parasequence 1 (fig. 2), using the CPS-1

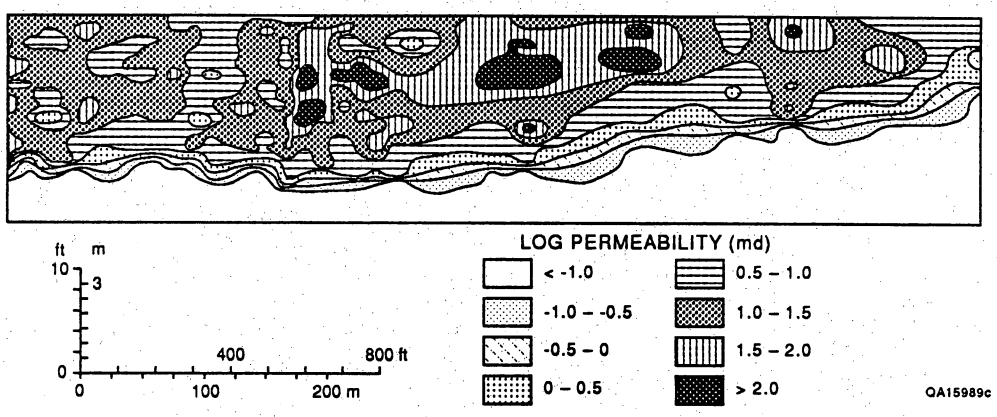

Figure 13. Permeability distribution for normalized parasequence 1 based on inverse-distance-squared contouring algorithm using CPS-1.

contouring package, shows extreme heterogeneity (fig. 13) within the bar-crest facies, bar-flank facies, and shallow-shelf facies, which are collectively referred to as the grainstone facies of parasequence 1.

To evaluate heterogeneity at different scales, permeability measurements from the different measurement grids were analyzed using variography. Within the bar-crest facies of parasequence 1, permeability transects were typically spaced 25 ft apart. Between transects A and Z (fig. 3), vertical transects were spaced 5 ft apart. Horizontal and vertical variograms of the permeability data indicate a short-range correlation range of about 3 ft in the vertical direction and a possible correlation range of about 30 ft in the horizontal direction (fig. 14a, b). In both cases, however, the spherical variogram indicates nugget constants of σ_0 = 0.15 md^2 and σ_0 = 0.35 md^2, respectively. This relatively large nugget indicates small-scale random variability of permeability. The small-scale random permeability variation is apparent in permeability patterns of the smaller scale grids, which were measured at regular 1-ft spacings (fig. 15) and at 1-inch spacings (not shown here). Variogram analysis of these small-scale permeability grids did not indicate a noticeable permeability correlation but showed a large variability in permeability. Measurement accuracy of the minipermeameter typically decreased toward the lower detection limit of 1 md and may have accentuated some of the observed noise in the permeability data. Extending the log spacing of the variogram (fig. 14c) shows the large-scale permeability pattern, characterized by nested structures. The range of these nested structures of about 400 ft is reflected in the overall permeability pattern shown in figure 13.

Using the fitted variogram models (fig. 14a, b), a kriged permeability map was constructed for the northern half of parasequence 1, consisting predominantly of bar-crest facies. Note that the kriged permeability map (fig. 16), based on the vertical permeability transects spaced 25 ft apart, shows a much smoother distribution than does the kriged permeability map based on the 1-ft grid (fig. 15).

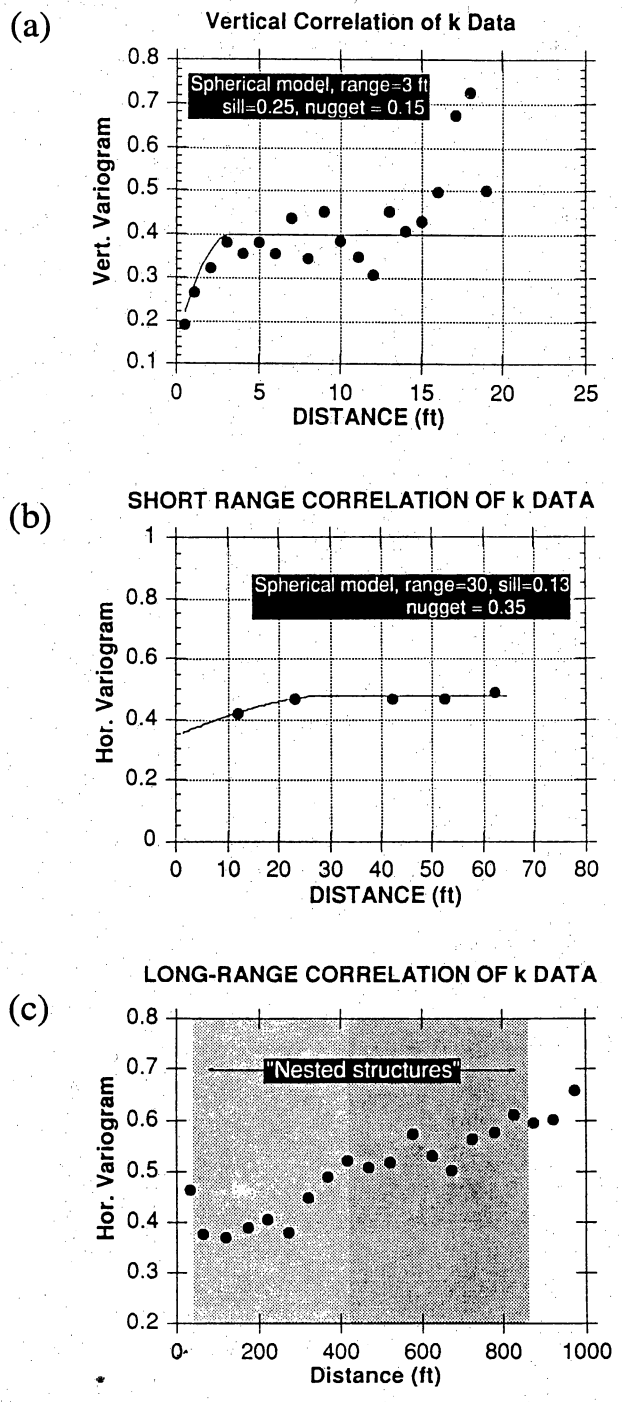

Figure 14. Sample variograms for the permeability transects from the grainstone facies in parasequence 1: (a) vertical variogram based on all transects, (b) short-range horizontal variogram, based on the 5-ft grid between sections A and Z (fig. 3), and (c) long-range horizontal variogram, based on all transects spaced between 25 and 100 ft.

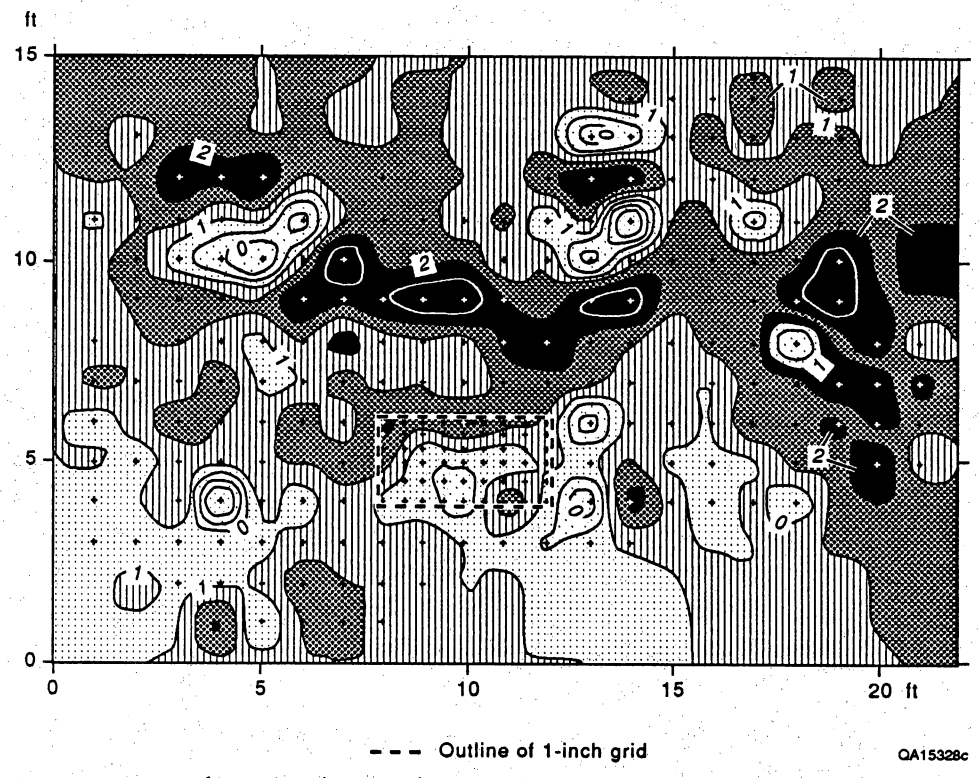

Figure 15. One-foot sampling grid in parasequence 1 with kriged permeability contours.

C. Conditional Simulation

Even though kriging can incorporate permeability correlation structures, it tends to average permeability over larger areas, ignoring small-scale heterogeneity. On the basis of the short-range correlation of permeability data (fig. 14), a series of stochastic permeability realizations were produced for the grainstone facies in parasequence 1. The model extends laterally from 0 to 1,050 ft and is 17 ft thick, with block sizes of 5 ft by 1 ft. The simulations, conditioned to permeabilities measured along vertical transects spaced approximately 25 ft apart (fig. 3), incorporate the correlation structure from the variograms (fig. 14a, b).

Two permeability distributions (realization nos. 7 and 11, table 1) out of 200 stochastic permeability realizations were selected for flow simulations, representing maximum and minimum lateral continuity (C_h) of domains having permeability values greater than 50 md (table 1). Comparison of the two permeability realizations (figs. 17a, b) does not show a noticeable difference. The ranges of 3 ft (vertical) and 30 ft (horizontal) (figs. 14a, b) are not immediately apparent in these realizations (fig. 17); the permeability patterns appear spatially uncorrelated because of the relatively large nugget, which is about the same magnitude as the sill (fig. 14). These conditional simulated realizations, however, preserve the spatial variability

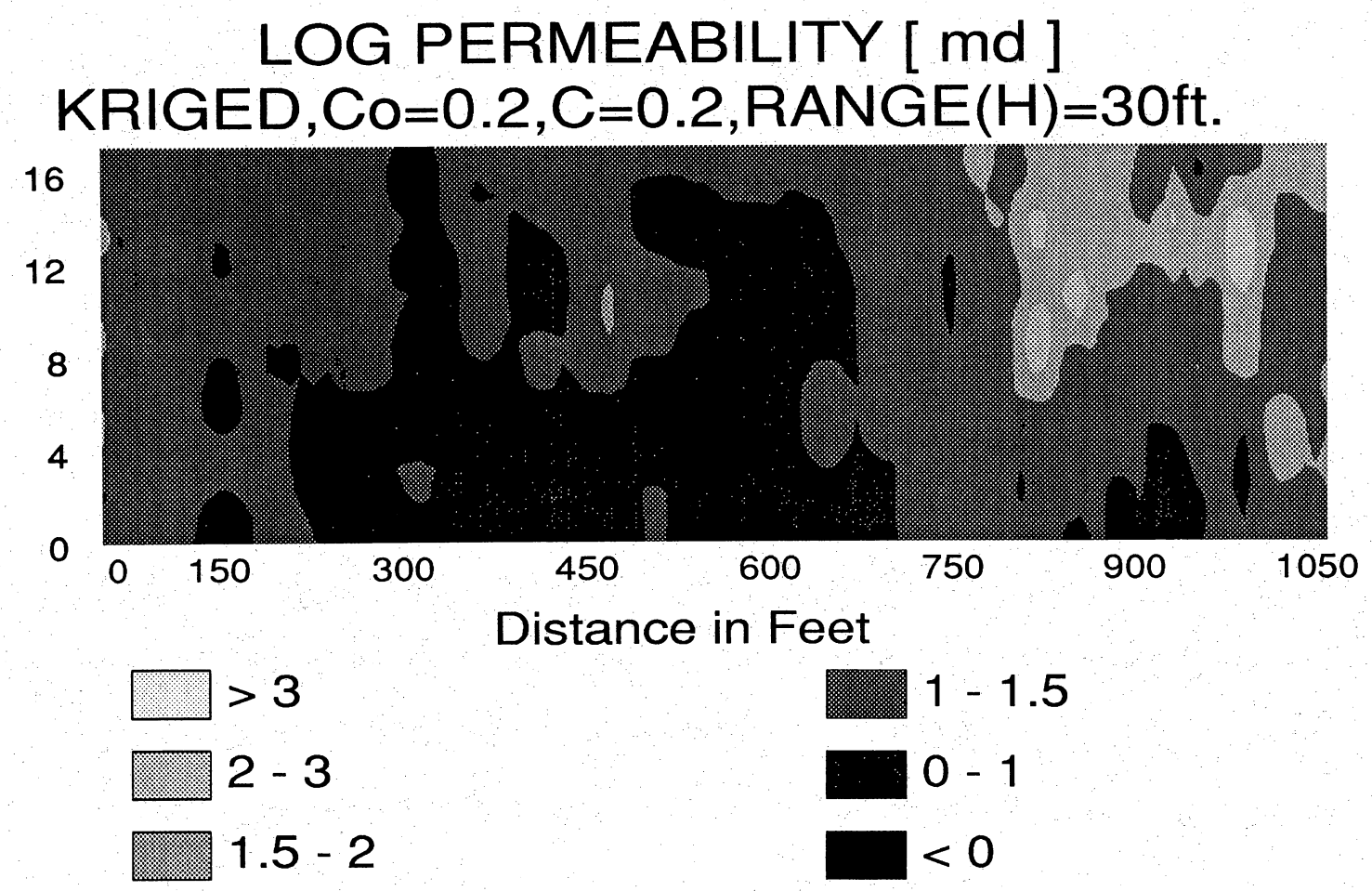

Figure 16. Kriged permeability distribution of the left part of parasequence 1, representing the bar-crest facies.

Table 1. Input parameters for waterflood simulations of grainstone facies in parasequence 1.

No.	Permeability realization	Statistics				Mean horizontal continuity ($\bar{C}_h$) (ft)
		Mean log-k (md)	Variance log-k (md^2)	Nugget (md^2)	Sill (md^2)	
1*	7	1.219	0.42	0.2	0.2	7.53
2	7	1.219	0.42	0.2	0.2	7.53
3	11	1.219	0.45	0.2	0.2	8.82
4	45	1.219	0.38	0.0	0.4	11.95
5	kriged	1.219	0.46	0.2	0.2	N/A
6*	facies-averaged	1.219	N/A	N/A	N/A	N/A

*Single relative-permeability and capillary-pressure curves.

Fluid properties:

Oil viscosity	1.000 cP
Oil density	55 lb/ft^3
Water density	64 lb/ft^3

exhibited in the variograms, whereas the kriged permeability map (fig. 16) averages out much of this variability.

As mentioned above, measurement uncertainty of the minipermeameter may have accentuated some of the observed noise in the permeability data, which is reflected in the relatively large nugget of the variograms (fig. 14). For comparison, unconditional permeability realizations were produced that incorporate the mean, variance, and variogram range but have a zero nugget and a sill of 0.4 md^2 and are not conditioned to the actual permeability values. All of these unconditional permeability realizations have mean continuity values that are higher than those of the conditional permeability realizations based on a 0.2-md^2 nugget. The unconditional realization 45 (fig. 18), which was selected on the basis of low continuity of relatively permeable zones, shows a smoother permeability pattern than that of a conditional permeability realization having a relatively high nugget (fig. 17). For comparison of waterflooding results, the different permeability realizations were corrected to the same mean permeability, which was equivalent to the data mean of log k = 1.219 md (table 1).

IV. WATERFLOOD SIMULATIONS OF PARASEQUENCE 1

A. Modeling Strategy

Waterflooding of the hypothetical two-dimensional reservoir was simulated by injecting water along the right boundary and producing along the left boundary. Injection and production were controlled by prescribed pressure conditions of 2,450 psi and 750 psi, respectively. A series of numerical simulations was performed to evaluate different effects associated with the observed heterogeneity on production characteristics. Flow simulations incorporating the observed heterogeneity were compared with those using a mean permeability to evaluate whether the observed

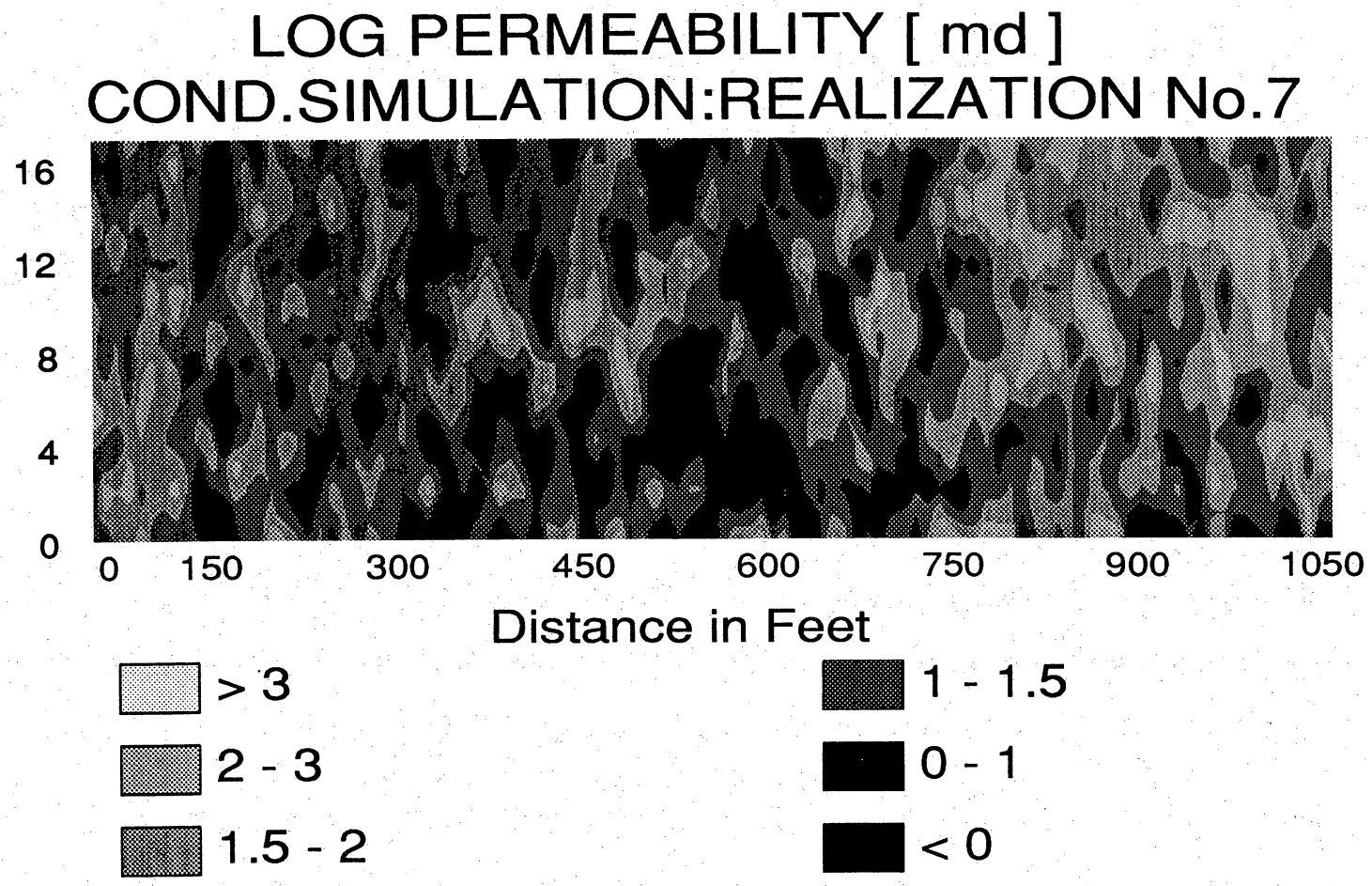

Figure 17. Conditional permeability distributions of (a) realization 7, representing lower continuity, and (b) realization 11, representing higher continuity of high-permeability zones.

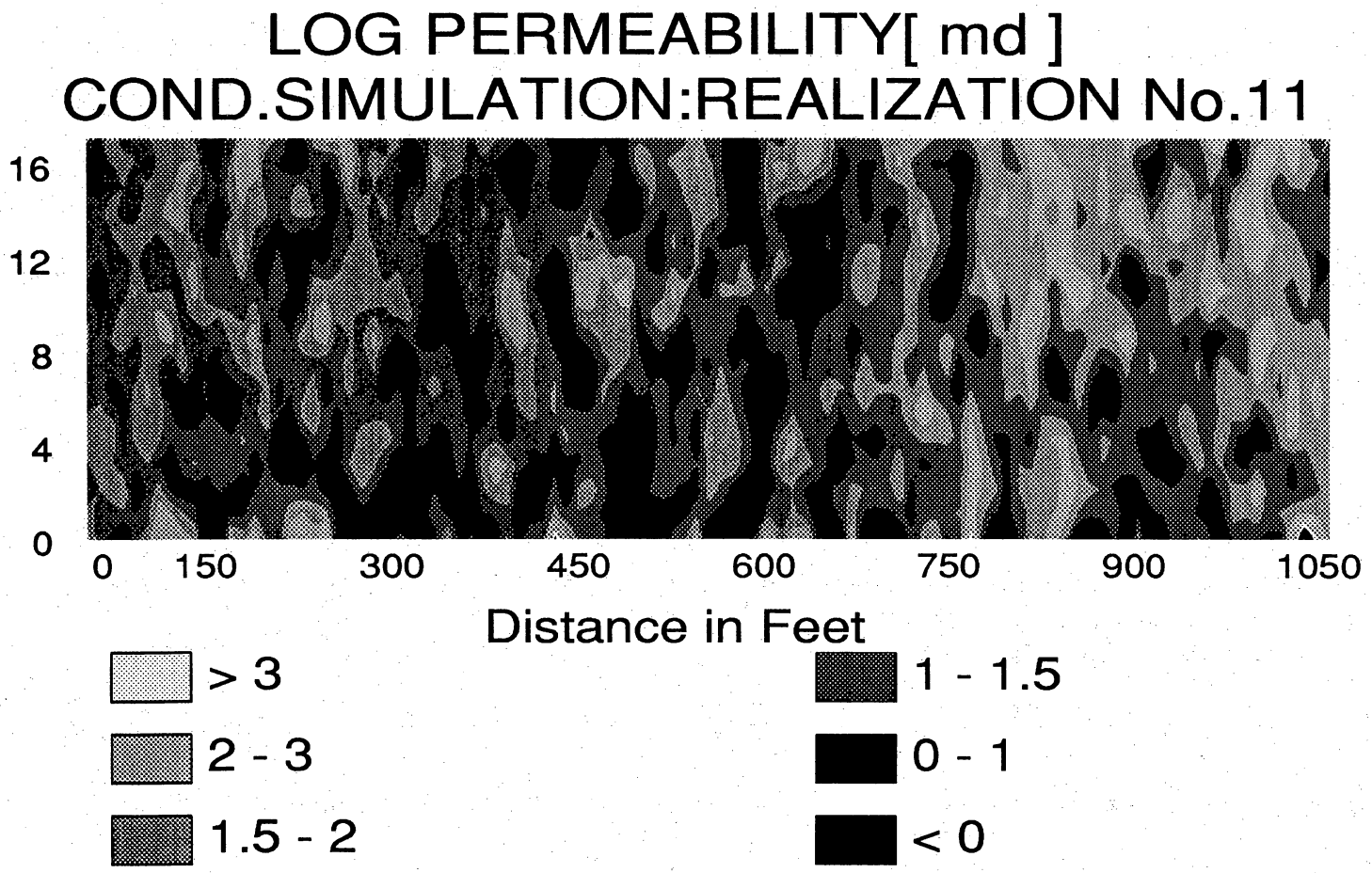
LOG PERMEABILITY[md]
COND.SIMULATION:REALIZATION No.11
16
12
8
4
0
0
150
300
450
600
750
900
1050
Distance in Feet
> 3
2 - 3
1.5 - 2
1 - 1.5
0 - 1
< 0

Figure 17b

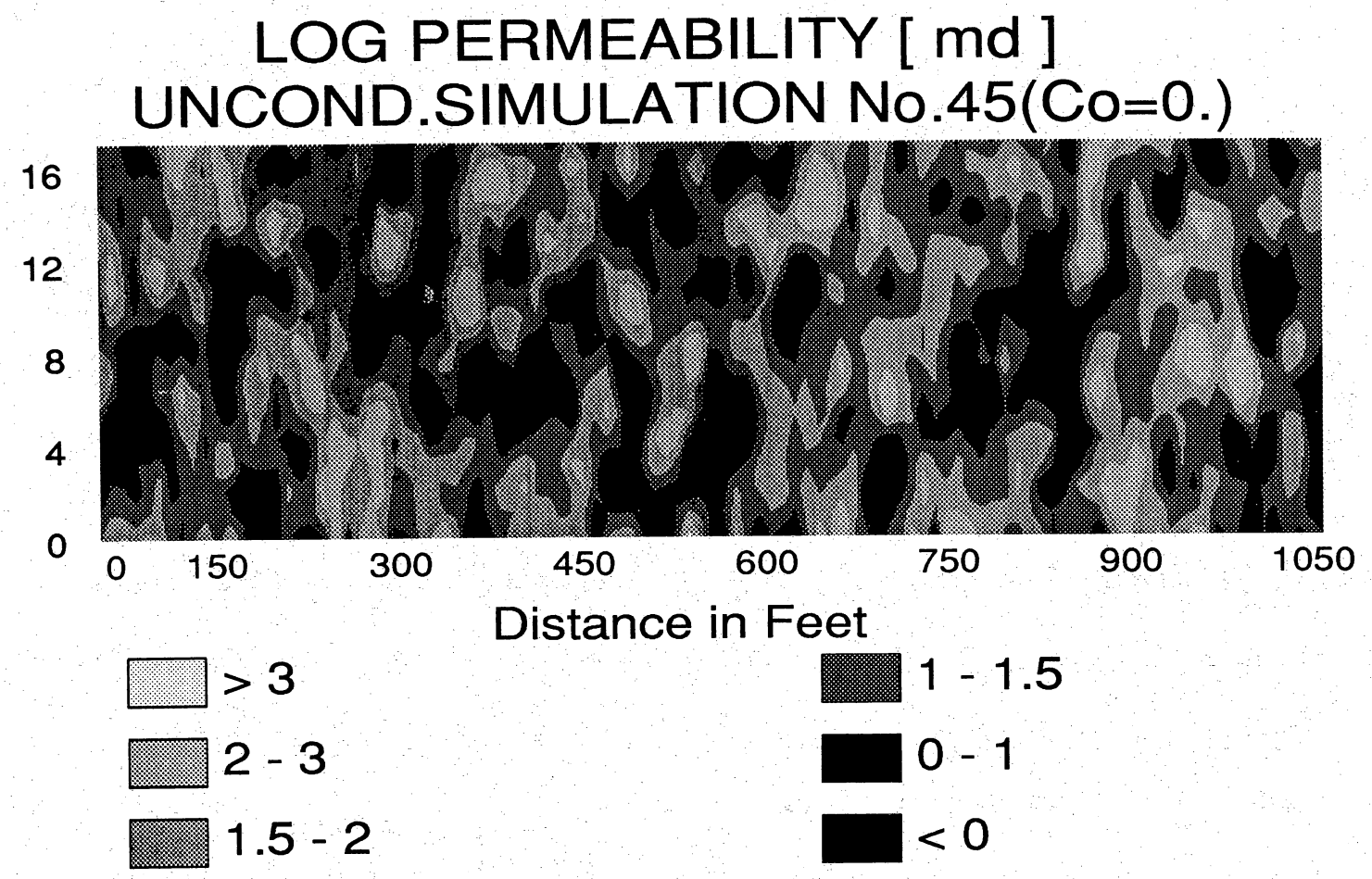

Figure 18. Unconditional permeability distribution of realization 45, representing low continuity of high-permeability zones.

permeability heterogeneity could be represented by a geometric-mean permeability and to determine the possible impact of short-range permeability correlation on production characteristics.

Input data for the simulator included the stochastic permeability distributions, porosities, and relative-permeability and capillary-pressure curves. Porosity-permeability relationships established on the basis of core-plug analyses for grainstones in parasequence 1 were used to calculate porosity distributions from the stochastic permeability realizations. The following empirical porosity-permeability relation is based on a linear transform representing intergranular pore characteristics in a grainstone (fig. 7a):

$$k = (5.01 \times 10^{-8})\, \phi^{8.33} \tag{1}$$

where k is absolute permeability (md) and ϕ is intergranular porosity (fraction). Similarly, an empirical relationship between water saturation, intergranular porosity, and capillary pressure, established for grainstones, was used to calculate capillary pressure as a function of water saturation and porosity of the grainstone facies in parasequence 1:

$$S_w = 68.581\, h^{-0.316}\, \phi^{-1.745} \tag{2}$$

where h represents capillary pressure expressed as the height of the reservoir above the free-water level. Initial water saturation as a function of porosity was computed using equation (2), assuming that the hypothetical reservoir is 500 ft above the free-water level. Residual oil saturation was assumed to be uniform at 25 percent.

The relative-permeability functions for oil and water were determined from the following equation (Honarpour and others, 1982):

$$k_{rw} = k^0_{rw} \left(\frac{S_w - S_{wr}}{1 - S_{or} - S_{wr}} \right)^{N_w} \tag{3a}$$

$$k_{ro} = k^0_{ro} \left(\frac{1 - S_w - S_{wr}}{1 - S_{or} - S_{wr}} \right)^{N_o} \tag{3b}$$

where S_{or} and S_{wr} are the residual oil saturation and the residual water saturation, respectively. The exponents N_w and N_o were derived from fitting relative permeability data obtained from grainstone fabric of two Dune Grayburg field cores. Both exponents were approximately 3 and were determined from the slope of the regression line representing the log of relative permeability versus the log of the normalized saturations in equations (3a) and (3b). Similarly, the relative-permeability endpoints and were derived from the intercepts of the log-log plots of the measured relative-permeability data versus saturation, which were 0.266 and 0.484, respectively, and correspond to residual oil saturation $S_{or} = 0.25$ and residual water saturation $S_{wr} = 0.1$, respectively.

Porosities derived from the different permeability realizations through the permeability-porosity transform in equation (1) typically range between 5 and 25 percent. Four relative-permeability and capillary-pressure curves representative of four porosity intervals were used: 5 to 10 percent, 10 to 15 percent, 15 to 20 percent, and 20 to 25 percent. For these porosity intervals, residual water saturations calculated from equation (2) were used to compute the relative-permeability curves according to equation (3). The relative-permeability and capillary-pressure curves used in the different flow simulations are shown in figures 19 and 20, respectively.

Six numerical simulations were run (table 1). Simulation nos. 1 and 6 used a single relative-permeability and a single capillary-pressure curve based on the arithmetic mean of porosity. The other simulations incorporated porosity-dependent relative-permeability and capillary-pressure curves (figs. 19, 20). The different simulations include (nos. 1 and 2) conditional permeability realization 7 (fig. 17a), representing low continuity of permeable zones; (no. 3) conditional permeability realization 11 (fig. 17b), representing high continuity of permeable zones; (no. 4) unconditional permeability realization 45 (fig. 18), representing low continuity of permeable zones assuming zero nugget; (no. 5) kriged permeability distribution (fig. 16); and (no. 6) uniform permeability distribution based on the geometric mean of measured permeability.

Computed water saturations of all simulations exhibited relatively sharp and vertical injection fronts despite the large variations in permeability, initial saturations, and capillary pressures in some simulations.

B. Simulation Results

Initial water saturation in simulation 1 (fig. 21) is uniform calculated from equation (2), using the arithmetic mean of porosity and assuming a reservoir height above the free-water level of 500 ft. Initial water saturation in simulation 2 is also calculated from equation (2), but by using variable porosity values computed from the porosity-permeability transform (fig. 7). This results in the uneven initial saturation distribution to the left of the water-injection front (fig. 22). Water saturations in the flooded zones are dependent upon capillary pressure as well as relative and absolute permeability. In simulation 1 (fig. 21) a single capillary-pressure curve and a single relative-permeability curve (figs. 19 and 20) were used, resulting in a much smoother saturation distribution than in simulation 2 (fig. 22). Despite the relatively heterogeneous permeability distribution, the water-injection front in both simulations is relatively sharp and approximately vertical.

Production characteristics of all six simulations are shown in figures 23 through 25. Each production curve for the different permeability realizations is characterized by an initial peak, followed by a gentle decline and then a rapid decline. The rapid decline represents the relatively sharp breakthrough of the water-injection front. Water breakthrough is dependent on the mean continuity of permeable zones in the stochastic permeability realizations. Water breakthrough in realization 11, representing high continuity of permeable zones, occurs earlier than that in realization 7, representing low continuity of permeable zones. Unconditional realization 45 has the highest mean horizontal continuity ($\overline{C}_h$ = 11.95 ft; table 1) and has an earlier

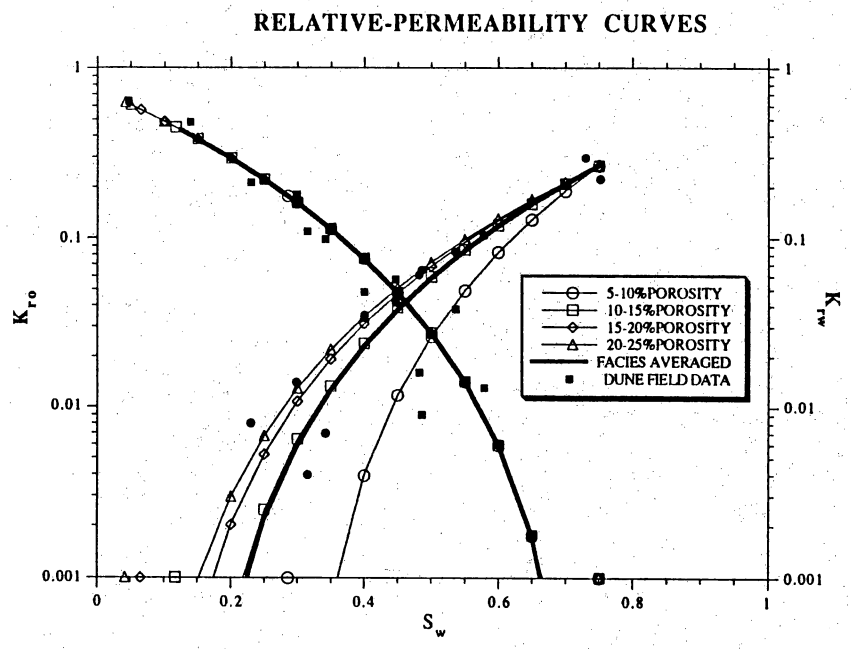

Figure 19. Relative-permeability curves used for the different waterflood simulations in parasequence 1.

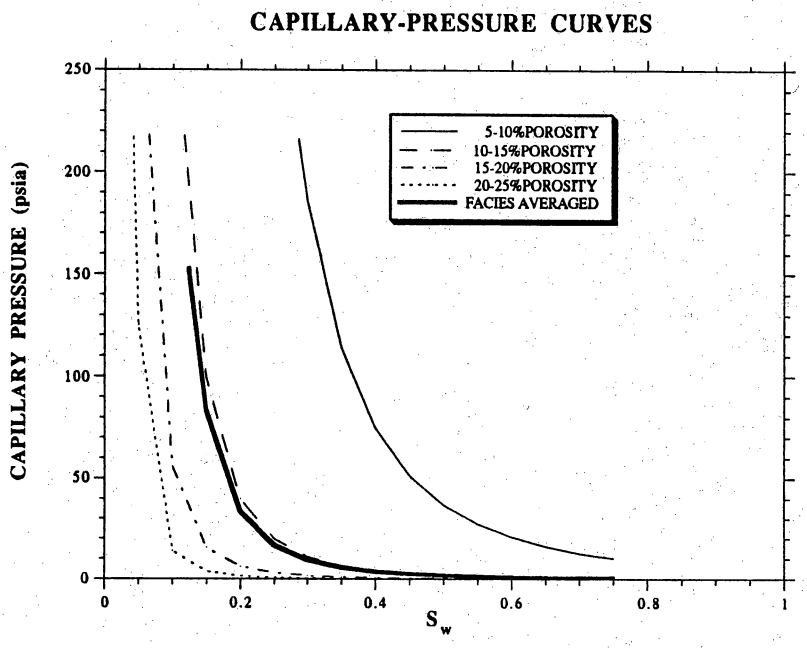

Figure 20. Capillary-pressure curves used for the different waterflood simulations in parasequence 1.

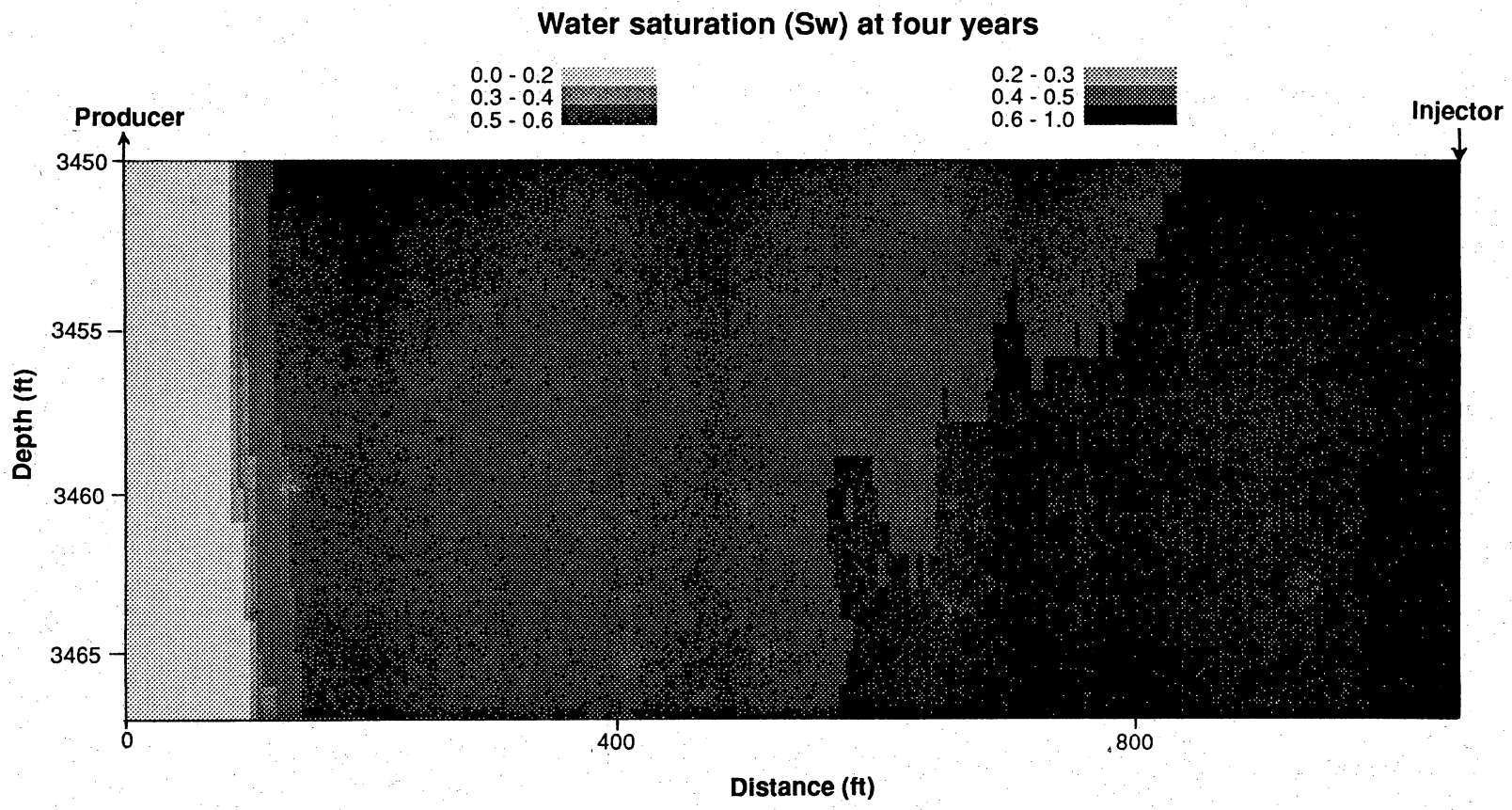

Figure 21. Computed water saturations for simulation 1 after injecting water for 4 yr, incorporating the permeability realization 7 (with uniform initial saturation and single relative-permeability and capillary-pressure curves based on arithmetic-mean porosity).

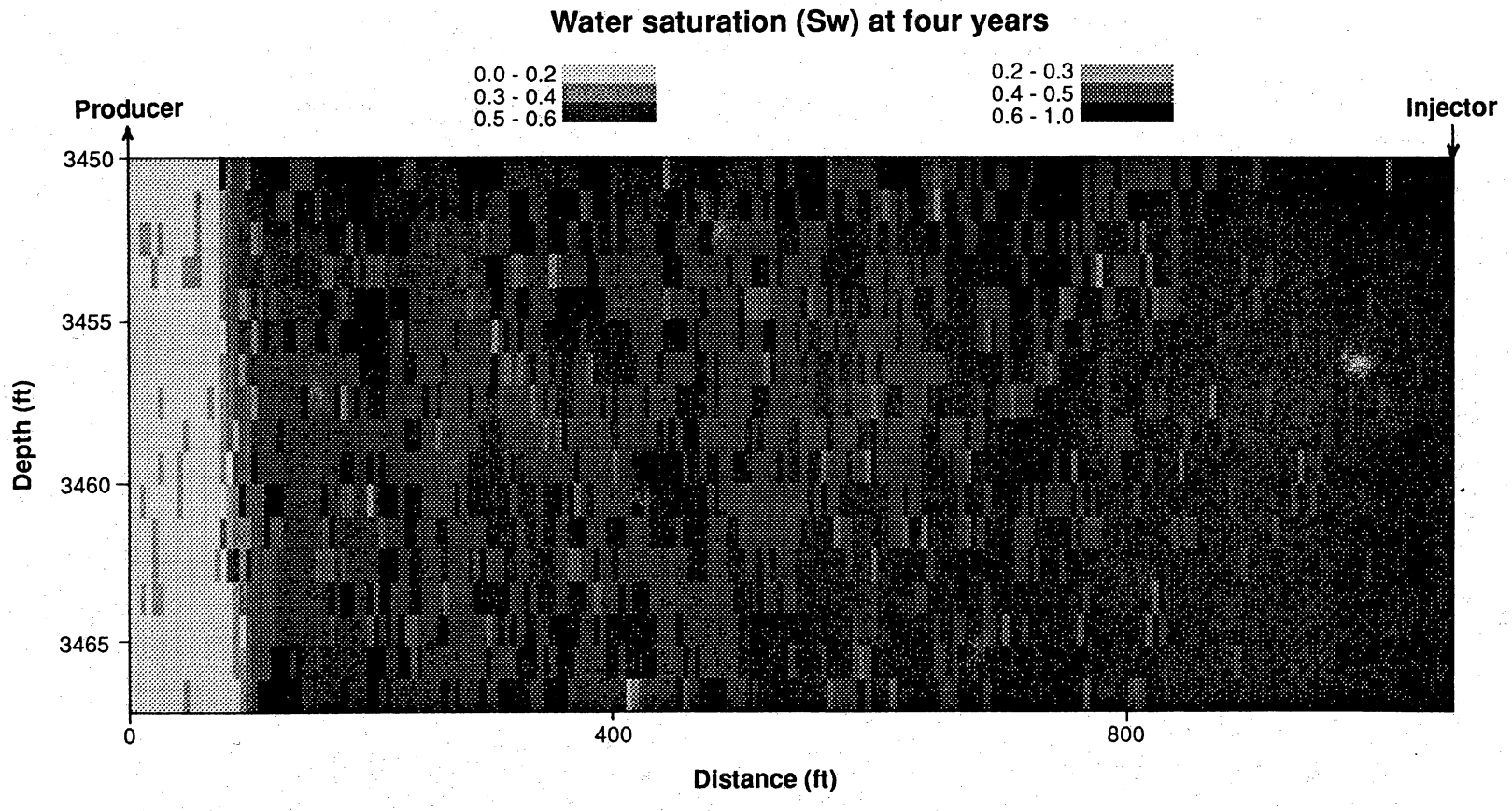

Figure 22. Computed water saturations for simulation 2 after injecting water for 4 yr, incorporating the permeability realization 7 (with relative-permeability curves and capillary-pressure curves dependent on porosity).

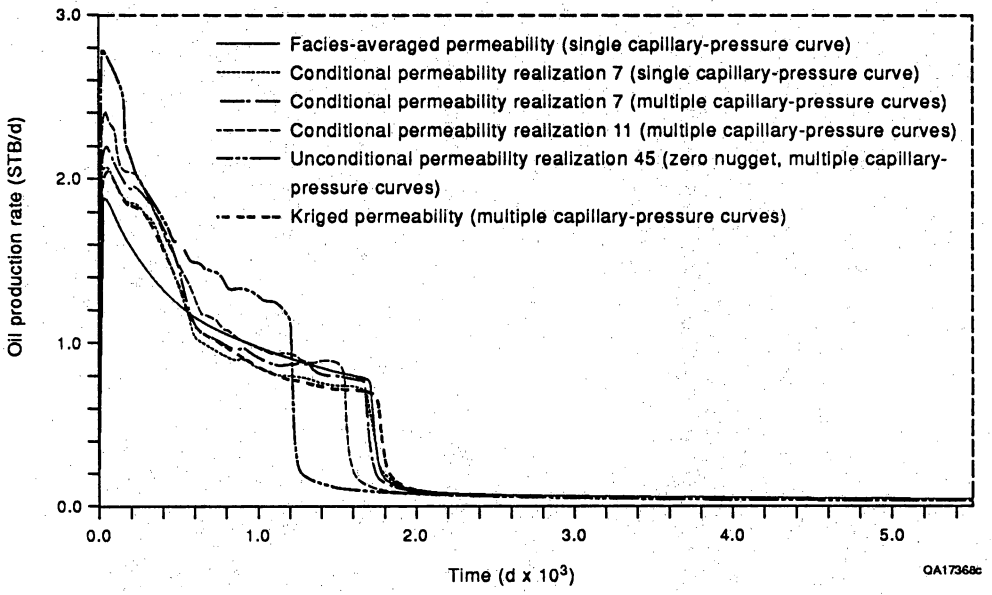

Figure 23. Oil-production rate versus time for waterflood simulations in parasequence 1.

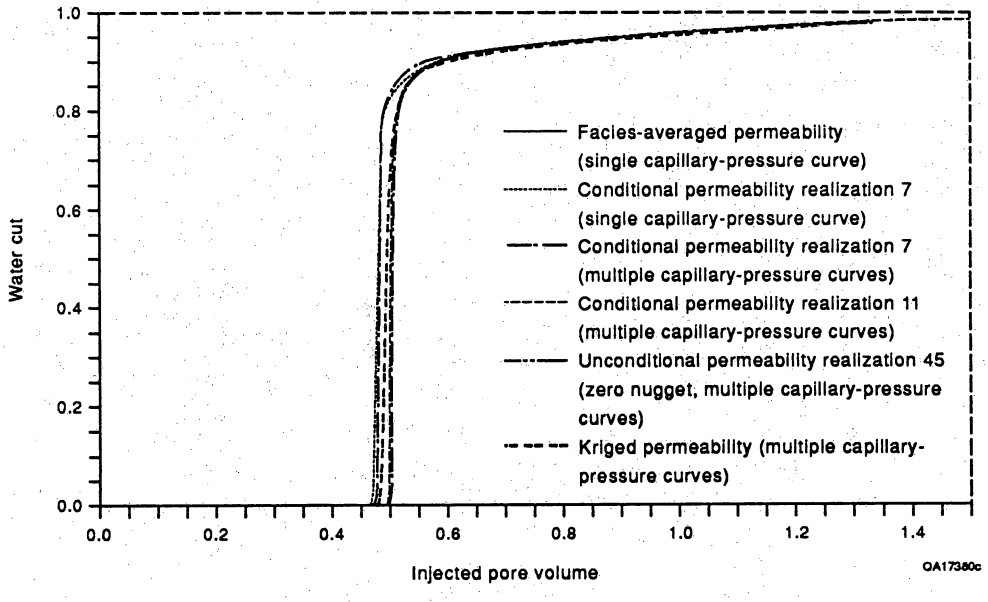

Figure 24. Water-oil ratio versus injected pore volumes for waterflood simulations in parasequence 1.

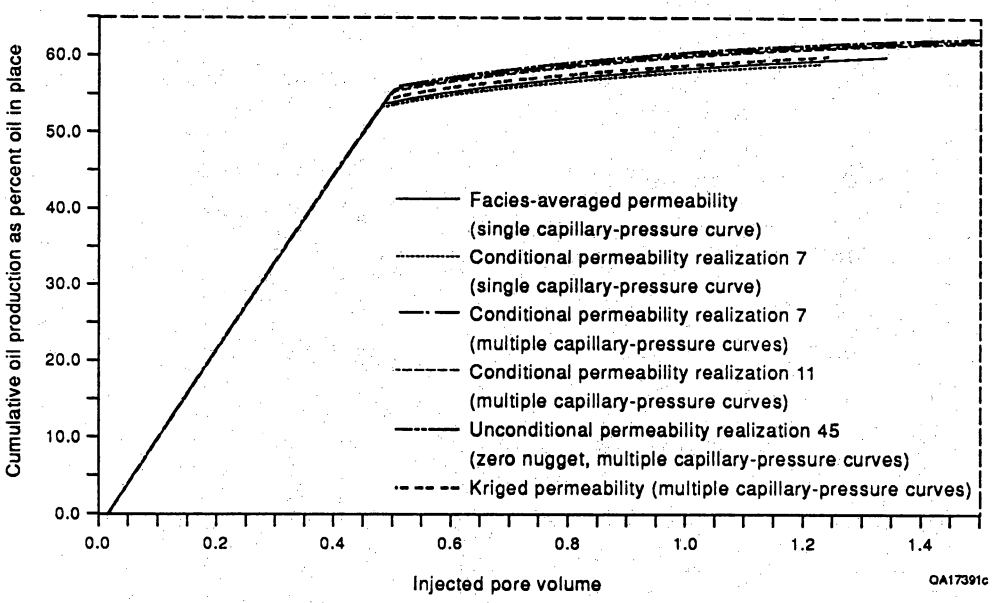

Figure 25. Cumulative oil production as percentage of original oil in place for waterflood simulations in parasequence 1.

breakthrough than any other simulation (fig. 23). Although unconditional realization 45, having a zero nugget, represents low continuity of permeable zones, its mean horizontal continuity is higher than that in realization 11, which represents high continuity of permeable zones but has a nugget of 0.2 md^2 (table 1). Higher continuity of relatively permeable zones results in higher interconnection of these zones and thus produces higher effective permeability than do permeability realizations characterized by low continuity (Fogg, 1989). As a result, unconditional permeability realization 45 shows the earliest water breakthrough because of the overall higher effective permeability. Also, the production curve of unconditional realization 45 illustrates the highest initial production rate but a subsequently steeper decline than production curves from the conditional permeability realizations (fig. 23). As with the water breakthrough, the initial production peaks of the stochastic permeability realizations are also dependent on the mean horizontal continuity.

The kriged permeability distribution shows a production curve similar to that of the conditional permeability realizations. This suggests that the larger scale permeability variation (fig. 16) controls the overall production characteristics and that the small-scale permeability variations incorporated into the stochastic permeability realizations have little importance (figs. 17 and 18). In comparison, the facies-averaged permeability distribution, which has no spatial permeability variation, indicates a smooth, approximately exponential production decline before the water breakthrough, which occurs at approximately the same time as that in the kriged and conditional permeability realizations.

Plotting water cut against injected pore volume shows nearly identical curves for the stochastic permeability realizations, incorporating porosity-dependent capillary-pressure curves (fig. 24). Simulation 1 with permeability realization 7,

incorporating a single capillary-pressure curve based on an arithmetic-mean porosity, and simulation 6 with the facies-averaged permeability distribution, incorporating a single capillary-pressure curve, show earlier water-breakthrough curves than those of the stochastic permeability realizations, incorporating porosity-dependent capillary-pressure curves (fig. 24). In comparison, the kriged permeability distribution falls between the two groups (fig. 24).

The sweep efficiency is improved using porosity-dependent capillary pressures, as indicated by the cumulative oil production as percent total oil in place (fig. 25). The waterflood simulations incorporating multiple capillary-pressure and relative-permeability curves (simulations 2 to 5) indicate higher sweep efficiency than those with single capillary-pressure and relative-permeability curves (simulations 1 and 6). Note that the sweep efficiency in simulation 5, representing the kriged permeability distribution, is slightly lower than the stochastic permeability realizations (simulations 2 to 4), indicating that the small-scale heterogeneity causes an increase in sweep efficiency.

C. Discussion

The effect of small-scale heterogeneity and associated capillary-pressure phenomena on cumulative production characteristics is relatively small and accounts for less than a 2.5 percent increase in sweep efficiency (fig. 25). For practical purposes, the observed heterogeneity within the grainstone facies in parasequence 1 can be represented by a geometric-mean permeability distribution using an arithmetic-mean porosity for calculating uniform initial water saturation and concomitant capillary pressure according to equation (2). However, production-rate history cannot be represented by a facies-averaged permeability distribution. The kriged permeability distribution (fig. 16) yields the same production-rate pattern as the conditional permeability realizations (fig. 23), indicating that small-scale permeability variability has a negligible effect on the production rate and only the large-scale permeability patterns need to be incorporated into the flow model for history matching.

Most hydrocarbon reservoirs typically consist of several different facies or rock-fabric units. The detailed geologic framework of the entire upper San Andres outcrop at Lawyer Canyon (fig. 2) is more typical of the complexity of subsurface reservoirs in a ramp-crest depositional environment than is parasequence 1 alone. One might expect that the production characteristics of this reservoir, composed of nine parasequences separated by discontinuous, tight mudstone layers, are more dependent on the spatial relationship of the different facies and flow barriers than on the permeability pattern within individual facies if significant heterogeneity does not occur within the facies. The above flow simulations indicate that even though permeability heterogeneity within individual facies exhibits some short-range correlation, it can be represented by a geometric-mean permeability distribution that, overall, yields the same cumulative production characteristics as those incorporating the observed permeability variability. To study the effects of larger scale features associated with the spatial distribution of different rock-fabric units on reservoir-flow behavior, waterflood simulations of the entire Lawyer Canyon outcrop model (fig. 2) were performed.

V. RESERVOIR-FLOW CHARACTERIZATION, LAWYER CANYON OUTCROP

A. Conceptualization of the Outcrop Reservoir-Flow Model

The geologic model of the Lawyer Canyon parasequence window (fig. 2), in conjunction with the rock-fabric characterization of the depositional facies (fig. 9), is the basis of the conceptual reservoir-flow model. Initial saturations for the different flow units were calculated using the porosity-saturation transforms for the three rock-fabric classes (fig. 8) and average porosities. It was assumed that the grainstones in parasequence 7, characterized by variable amounts of separate-vug porosity, (fig. 7b) have the same porosity-saturation relationship as the nonvuggy grainstones in parasequences 1, 2, 3, and 9 (fig. 9). The effect of vuggy porosity was accounted for by assigning a higher residual oil saturation to the grainstones in parasequence 7.

The constructed reservoir flow model distinguishes 11 flow units that have different average permeability, porosity, initial water saturation, and residual oil saturation (table 2). The flow model is discretized in 4,089 irregularly shaped grid blocks, representing the spatial distribution and the petrophysical properties of the different rock fabrics and depositional facies (table 2). Reservoir block sizes are 100 ft in the horizontal direction and have variable thickness in the vertical direction, ranging from less than 0.5 ft to several feet. The constructed reservoir model incorporates the general geometry and the spatial distribution of the different facies mapped in the outcrop, as shown by the distribution of initial water saturation of the discretized flow units (fig. 26).

Relative permeabilities for the different flow units are based on the shapes of relative-permeability curves derived from fitting relative-permeability data obtained from cores in the Dune field, West Texas. Similar to the relative-permeability curves in figure 19, the fitted curves were adjusted to the computed initial water saturations and to the residual oil saturations of the different flow units (table 2). Although the shape of the relative-permeability curves was obtained by fitting relative-permeability measurements from grainstone cores from the Dune field reservoir, West Texas (fig. 19), the same curve shapes were used in this study not only for the grainstone rock fabrics but also for the grain-dominated packstone and mudstone/wackestone rock fabrics. Only the relative-permeability endpoints were adjusted according to the computed initial water saturations and assumed residual oil saturations.

Capillary-pressure curves were calculated on the basis of average porosities and rock-fabric classifications of the different flow units. In addition to the porosity-dependent saturation–capillary-pressure relationship for grainstones (eq. 2), the following relationships are used for the other two rock-fabric classes:

$$\text{Grain-dominated packstone} \qquad S_w = 106.524\, h^{-0.407}\, \phi^{-1.440} \qquad (4)$$

$$\text{Mudstone-wackestone} \qquad S_w = 161.023\, h^{-0.505}\, \phi^{-1.2104} \qquad (5)$$

Table 2. Properties of rock-fabric flow units for Lawyer Canyon outcrop reservoir model.

Flow units	Rock fabric	Depositional facies	Porosity (arithm. average)	Permeability (geometric average, md)	Initial water saturation	Residual oil saturation
1	Mudstone	Flooded shelf Tidal flat	0.04	0.01	0.9	0.01
2	Wackestone	Shallow shelf I	0.105	0.30	0.405	0.4
3	Grain-domin. packstone	Shallow shelf I	0.085	4.50	0.214	0.35
4	Grain-domin. packstone	Shallow shelf II Bar top	0.129	1.80	0.40	0.35
5	Grain-domin. packstone	Shallow shelf II	0.118	5.30	0.243	0.35
6	Grainstone (moldic)	Shallow shelf II	0.145	0.7	0.091	0.40
7	Grainstone (moldic)	Shallow shelf I Shallow shelf II Bar crest Bar top	0.159	2.2	0.077	0.40
8	Grainstone (highly moldic)	Shallow shelf II Bar crest Bar-accretion sets	0.23	2.5	0.041	0.40
9	Grainstone	Bar flank	0.095	9.5	0.189	0.35
10	Grainstone	Bar crest Bar-accretion sets	0.11	21.3	0.147	0.25
11	Grainstone	Bar crest	0.135	44.0	0.103	0.25

Fluid properties:

Oil viscosity	1.000 cP
Water viscosity	0.804 cP
Oil density	55 lb/ft^3
Water density	64 lb/ft^3

where h is the height of the reservoir above the free-water level (ft) and ϕ is the porosity (fraction).

In a series of waterflood simulations, various factors affecting reservoir-flow behavior were examined (table 3) using the ECLIPSE reservoir simulator. Simulation EC-A represents the base scenario, which is used to describe waterflooding in this reservoir model. Production characteristics of simulation EC-A were compared with those from other simulations to evaluate effects of capillary pressures (simulation EC-B), model conceptualization (simulations EC-N and EC-DP), and different injection practices (simulations EC-R and EC-F).

B. Simulation Results

Waterflooding of the Lawyer Canyon outcrop reservoir model was simulated by injecting water through a fully penetrating well along the right side of the model

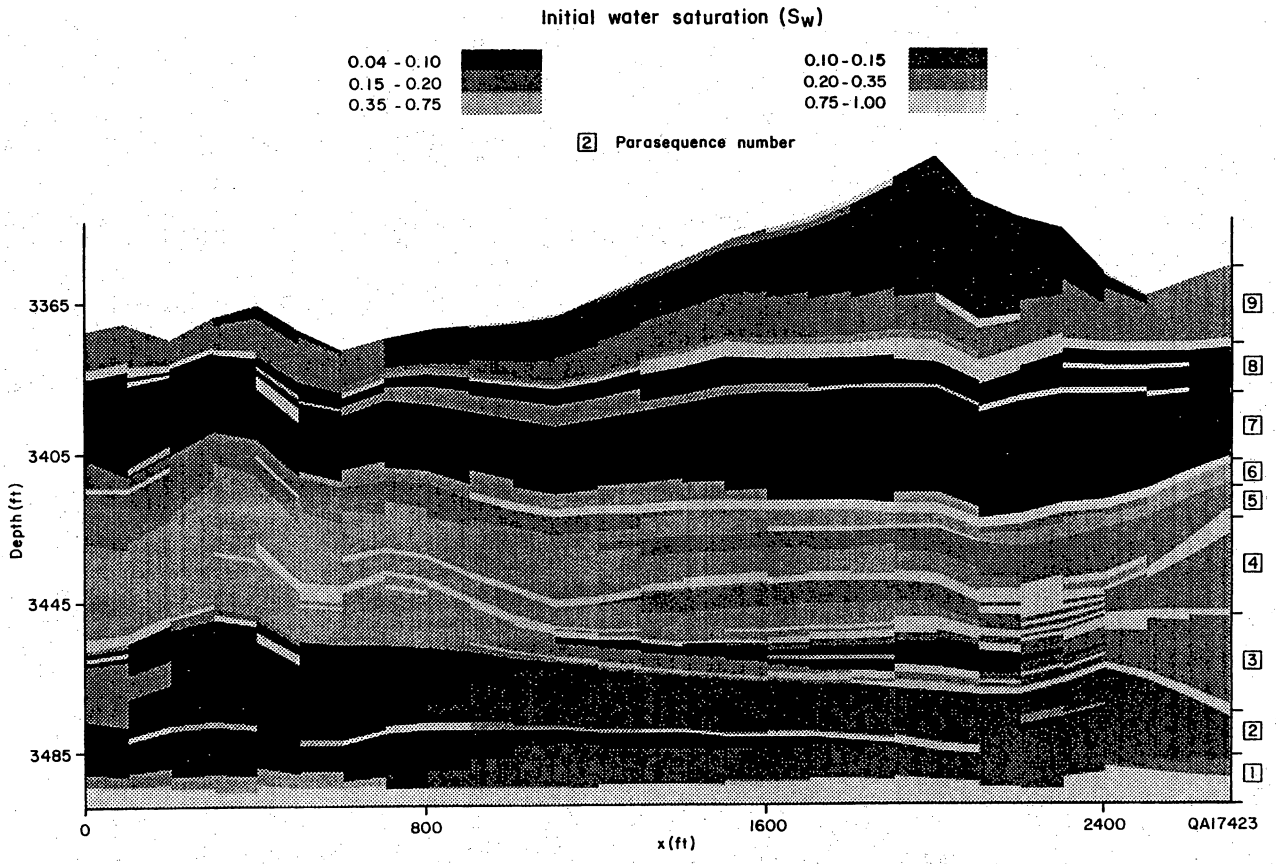

Figure 26. Initial water saturation of the flow units of the outcrop model.

Table 3. Waterflood simulations of the Lawyer Canyon outcrop model.

Sim. no.	Model scenario: Grid	Production well location	Capillary pressure	Permeability data
EC-A	Irregular	Right	Yes	Facies-averaged
EC-B	Irregular	Right	No	Facies-averaged
EC-N	Normalized	Right	Yes	Facies-averaged
EC-DP	Normalized	Right	Single	Linear interpol. between wells
EC-R	Irregular	Left	Yes	Facies-averaged
EC-F	Irregular	Middle	Yes	Facies-averaged

and by producing from a well at the left side (fig. 26) The injection and production rates were controlled by prescribed pressures of 4,350 psi and 750 psi, respectively.

The computed change in water saturation for simulation EC-A after water injection of 20 yr (fig. 27a), 40 yr (fig. 27b), and 60 yr (fig. 27c) demonstrates that the high-permeability grainstone rock-fabric units in parasequences 1, 2, and 9 are preferentially flooded. Furthermore, flooding is controlled by the relatively tight mudstone units separating most of the parasequences. The grainstone facies in parasequences 7 and 8 are characterized by lower permeabilities and higher porosities than those in parasequences 1, 2, and 9, owing to separate-vug porosity (table 2); consequently, the water-injection front does not advance as far as that in parasequence 9 (fig. 27). However, the water-injection front in parasequences 3 through 6 appears to have advanced farther than that in parasequences 7 and 8, although the permeability of the predominantly wackestone rock fabrics in parasequences 3 through 6 is lower than that of the moldic grainstone rock fabrics in parasequence 7. This indicates that the movement of the displacement front is not only affected by the permeability contrast but inversely related to porosity.

In the upper right of the model, the change in computed water saturation after 40 and 60 yr indicates cross flow of water from parasequence 9 into parasequence 7, thereby bypassing the injection front within parasequences 7 and 8. As a result, an area of unswept, mobile oil develops in the right part of the model, as shown by the computed water saturation distribution after 60 yr of waterflooding (fig. 28). This mobile oil is trapped by cross flow even though the mudstone layers, having a permeability of 0.01 md, represent the parasequence boundaries and are continuous in this area.

The production characteristics of simulation EC-A and the other simulations (table 3) are shown in figure 29 (production rate), figure 30 (water cut), and figure 31 (cumulative production as percent oil in place). Comparison of the production characteristics of the different simulations were used to evaluate various factors affecting reservoir-flow behavior.

1. Effect of Capillary Pressure

In the first test, effects of capillary pressure were studied. Simulation EC-B does not incorporate capillary pressures (table 3). Production rates in simulation

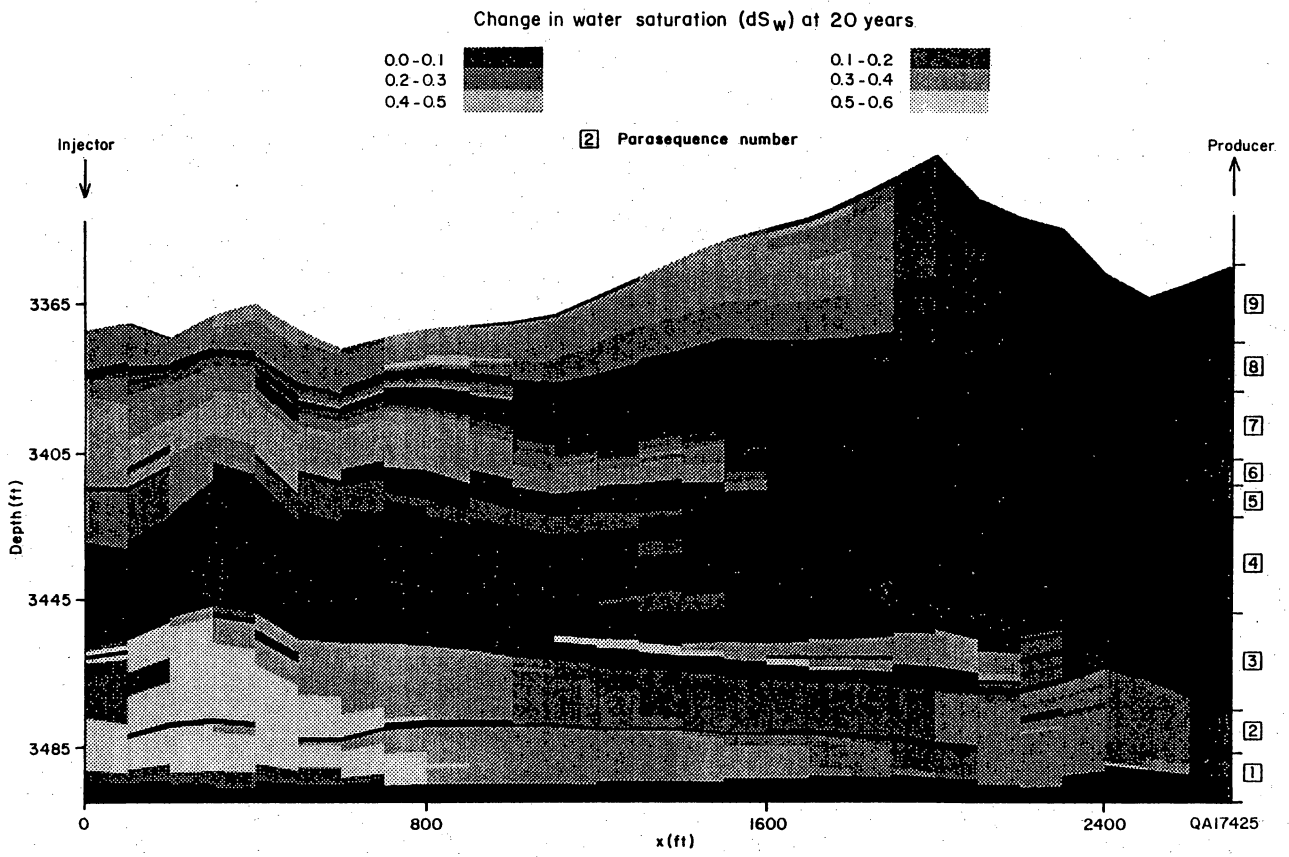

Figure 27. Computed changes in water saturation for simulation EC-A after waterflooding of (a) 20 yr, (b) 40 yr, (c) 60 yr.

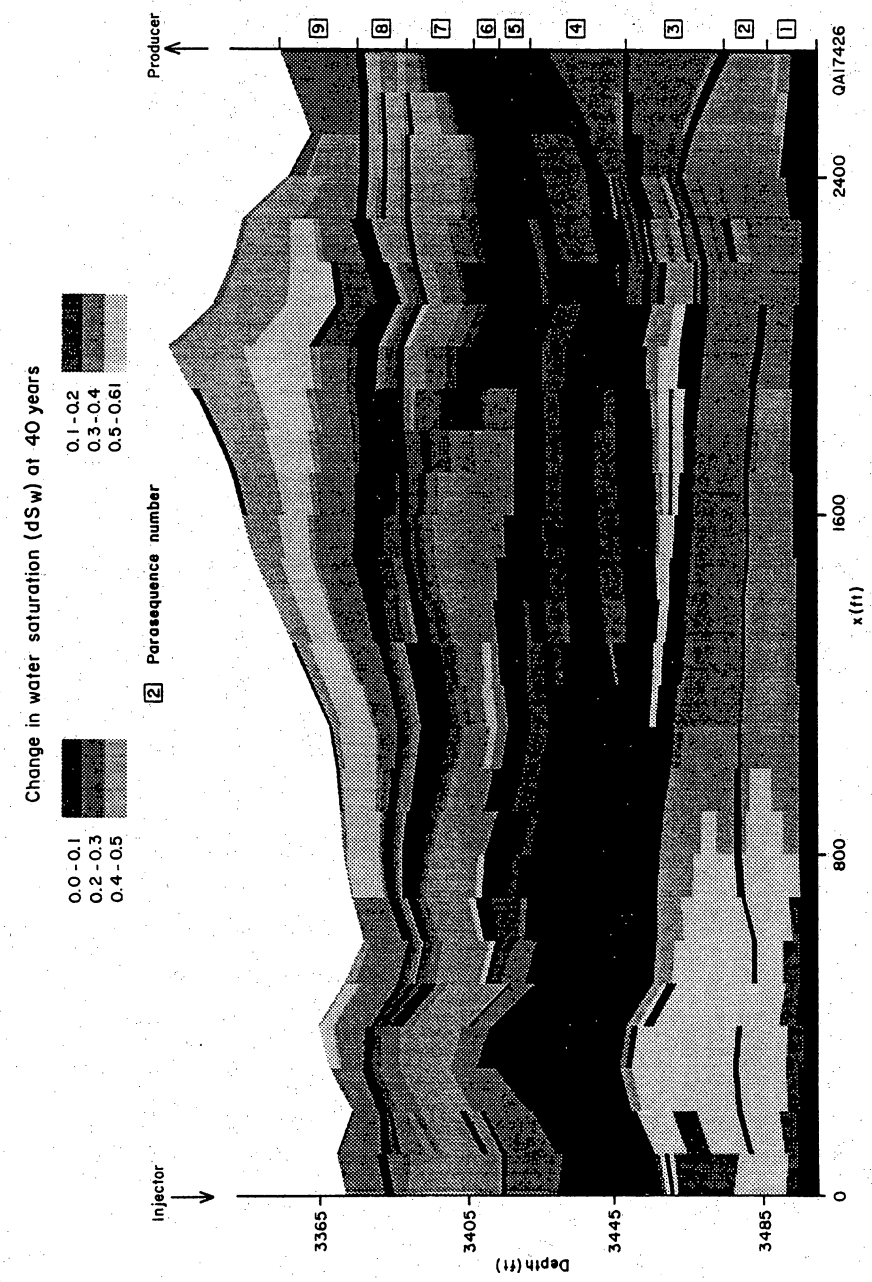
Change in water saturation (dSw) at 40 years
0.0 - 0.1
0.2 - 0.3
0.4 - 0.5
0.1 - 0.2
0.3 - 0.4
0.5 - 0.61
2 Parasequence number
Injector
Producer
9
8
7
6
5
4
3
2
1
3365
3405
3445
3485
Depth (ft)
0
800
1600
2400
x (ft)
QA17426

Figure 27b

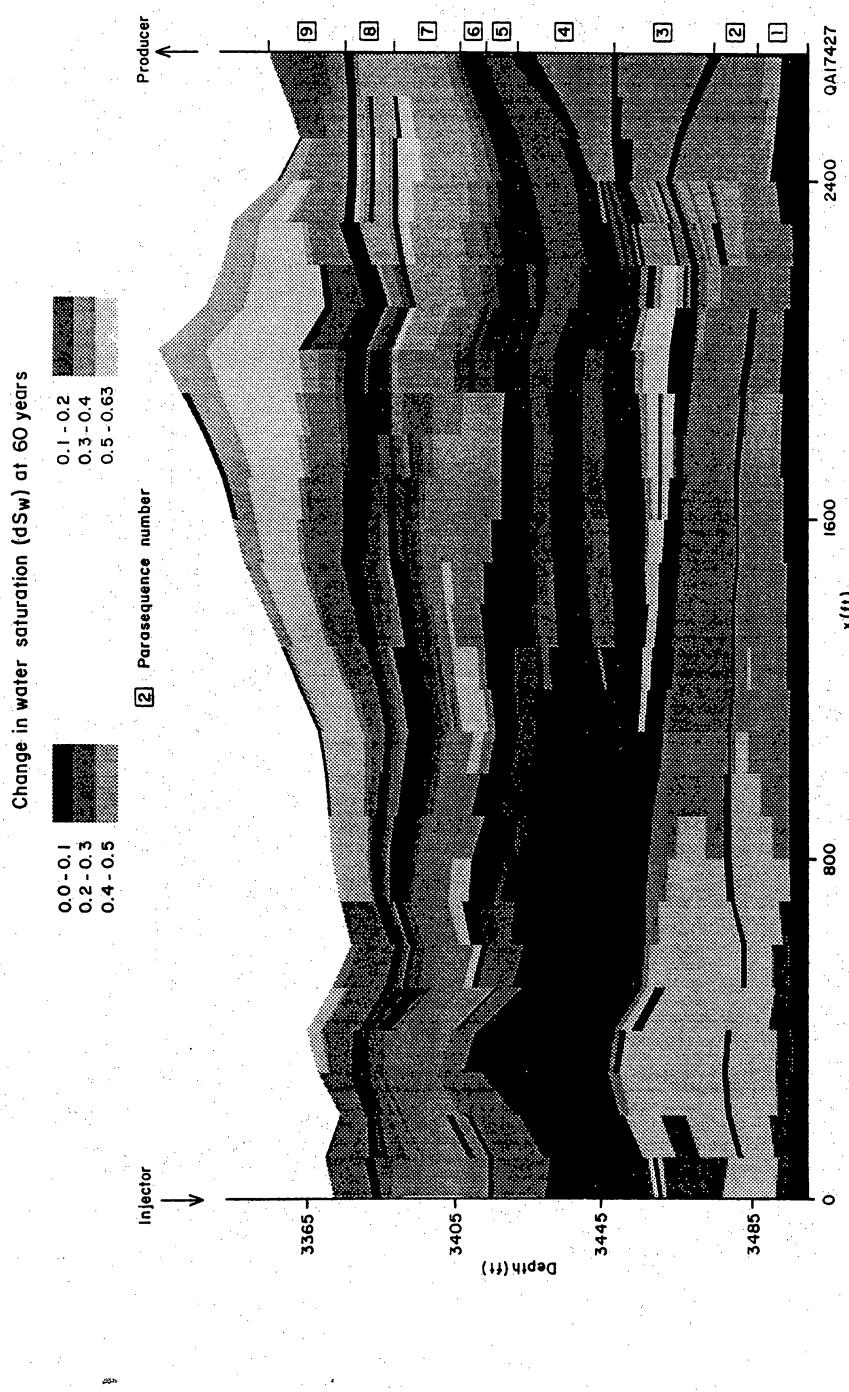
Change in water saturation (dSw) at 60 years
0.0 - 0.1
0.2 - 0.3
0.4 - 0.5
0.1 - 0.2
0.3 - 0.4
0.5 - 0.63
Parasequence number
Injector
Producer
Depth (ft)
3365
3405
3445
3485
0
800
1600
2400
x (ft)
QA17427

Figure 27c

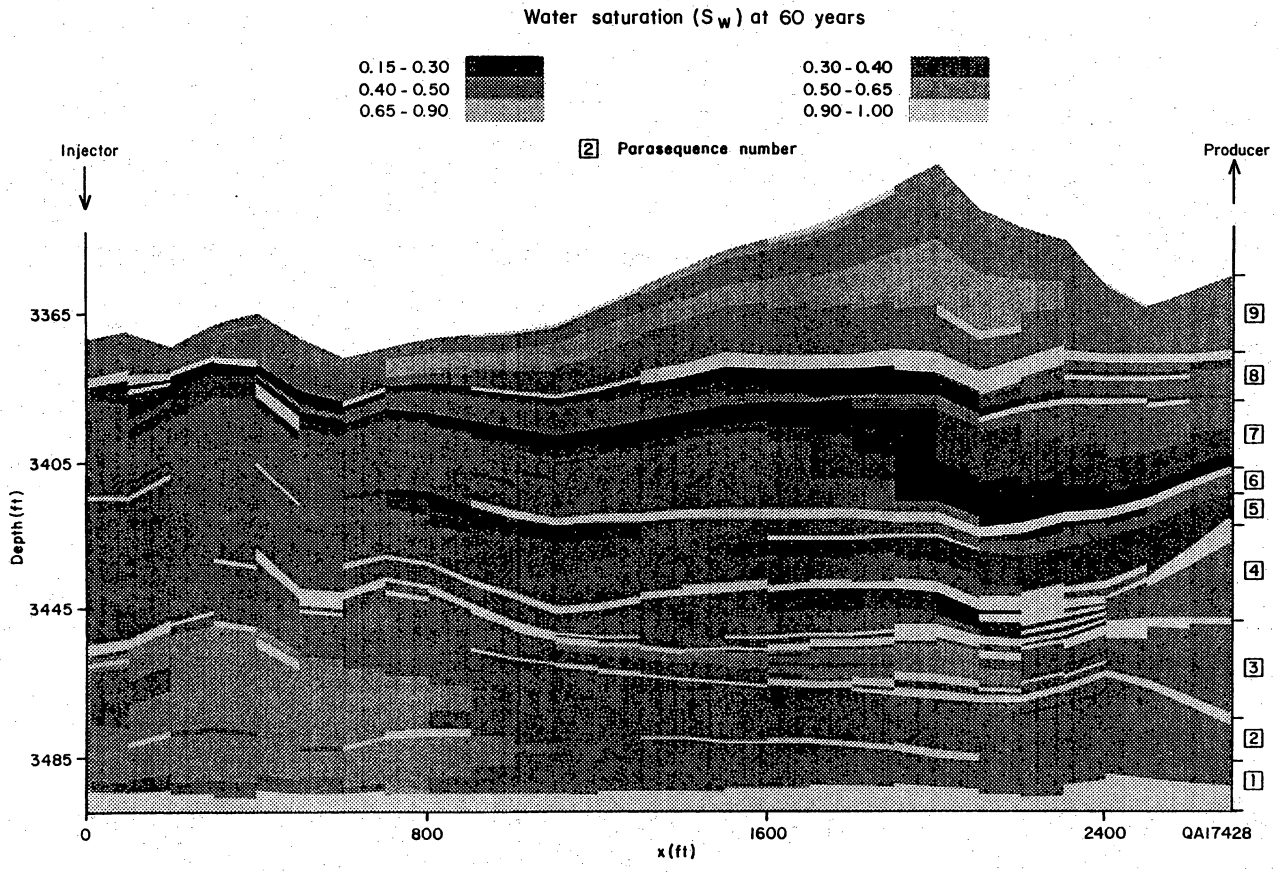

Figure 28. Computed water saturation for simulation EC-A after water injection of 60 yr.

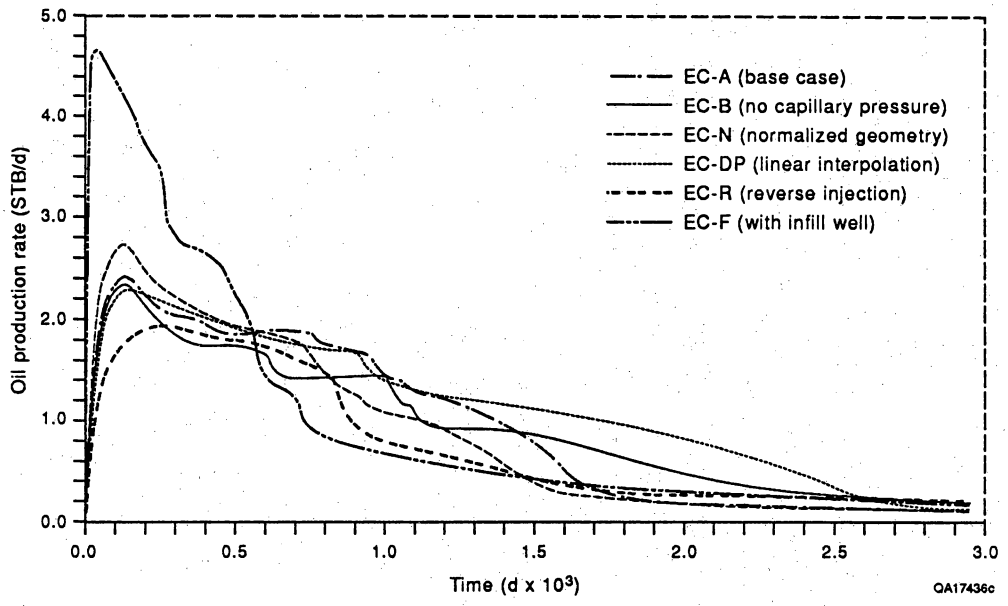

Figure 29. Oil-production rate versus time for simulations of the Lawyer Canyon outcrop model.

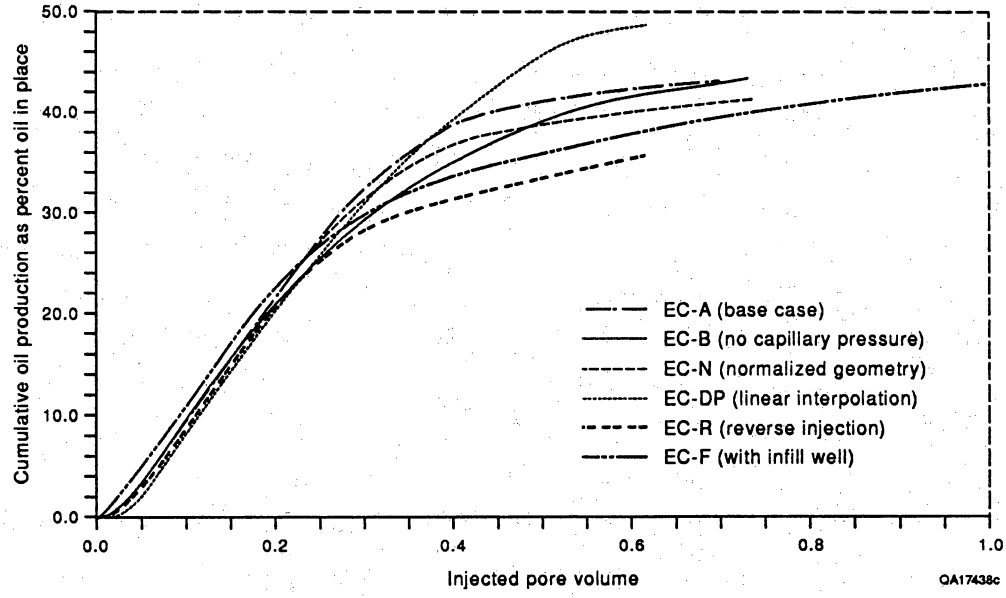

Figure 30. Water-oil ratio versus injected pore volume for simulations of the Lawyer Canyon outcrop model.

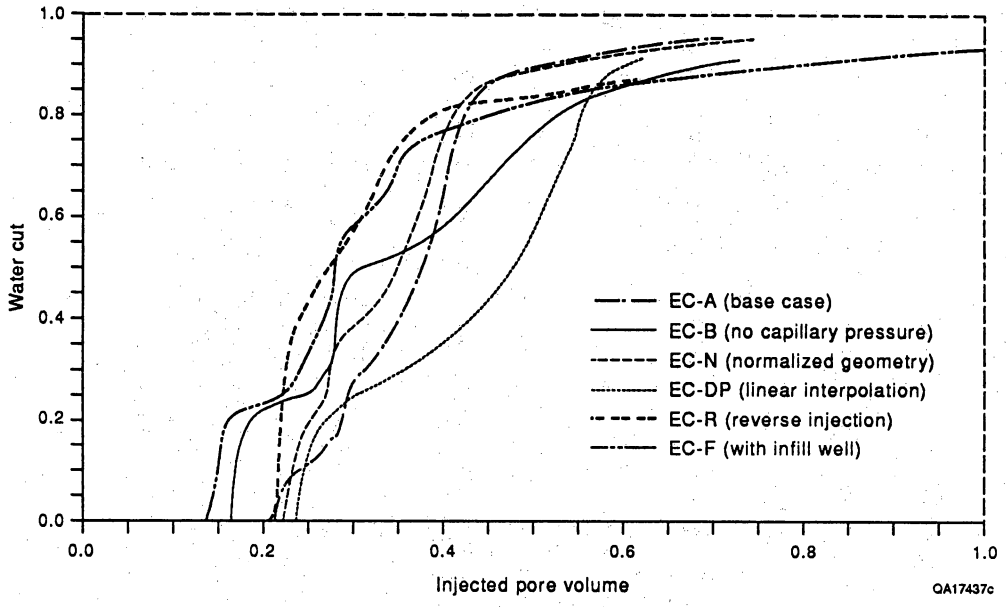

Figure 31. Cumulative oil production as percentage of original oil in place for simulations of the Lawyer Canyon outcrop model.

EC-B show a more stepwise decline with time, reflecting the flooding of the grainstone-dominated parasequences, as compared with production characteristics of the base case in simulation EC-A (fig. 29). Production rates are initially lower than those in simulation EC-A, but simulation EC-B maintains higher rates after 16,000 days. The stepwise decline in production rate is also reflected in the stepwise increase in water cut (fig. 30). Neglecting capillary pressures results in a lower seep efficiency, as shown by the cumulative production curve (fig. 31). In simulation EC-A, capillary pressure improves sweep of the less permeable zones in parasequences 3 through 6, whereas in simulation EC-B, waterflooding is restricted to the more permeable grainstone facies in parasequences 1, 2, 7, and 9. Ultimate oil recovery of the two simulations, however, is the same (fig. 31).

2. Effect of Model Conceptualization

The effect of irregular formation geometry as compared with that of normalized formation geometry was evaluated in simulations EC-N and EC-DP (table 3). In simulation EC-N, the nine parasequences were normalized to a constant thickness, approximating the spatial distribution of the mapped facies (fig. 2). Production rates are initially higher than those in simulation EC-A, but they drop off more rapidly (fig. 29). The water-breakthrough curve for the normalized reservoir model (simulation EC-N) is steeper than that in simulation EC-A (fig. 30) and shows a lower recovery efficiency (fig. 31).

In simulation EC-DP, the reservoir model was constructed using the permeabilities of the individual flow units at the injection and production wells and

then linearly interpolating permeability between wells using the normalized grid from simulation EC-N. This scenario represents a typical reservoir model constructed from well data, where the facies and permeability distributions of the interwell area are unknown. When using well data from only the left and right sides of the outcrop model (fig. 2), the relatively permeable grainstone facies in parasequence 9 is not incorporated into the layered model. Furthermore, only a single relative-permeability curve and a single capillary-pressure curve are used in simulation EC-DP.

Initial production rates in simulation EC-DP are similar to those in simulation EC-A but do not show the drop off after about 16,000 days (fig. 29), which is reflected in a less steep water-breakthrough curve than that in simulation EC-A (fig. 30). More importantly, sweep efficiency is overestimated in this layered model (fig. 31).

3. Effect of Injection Practice

Two additional flow scenarios were simulated to evaluate the effects of different injection schemes (table 3). In simulation EC-R, injection and production is reversed when the reservoir is flooded from the right side. Although the reservoir model and properties are the same in simulation EC-R and in EC-A, the production characteristics are noticeably different. Initial production rates in simulation EC-R are lower than those in simulation EC-A (fig. 29), but they remain slightly higher after 16,000 days. That is, at later times simulation EC-R produces at a lower water-oil ratio, which is characterized by the water-cut curve that levels out at a lower value than that of simulation EC-A (fig. 30). Sweep efficiency is significantly lower in simulation EC-R than in simulation EC-A (fig. 31), indicating that the spatial distribution of permeable grainstone facies relative to the direction of the waterflood (fig. 2) is important for the overall reservoir-flow behavior.

Comparing the change in water saturation after 40 yr of waterflooding shows a much larger area of unswept oil in the center of the model in simulation EC-R (fig. 32) than in simulation EC-A (fig. 27b). More importantly, cross flow occurs on the left side of the model toward the production well in simulation EC-R (fig. 32), from parasequence 9 all the way to parasequences 1 and 2. Although parasequences 3 through 6 are composed predominantly of less permeable wackestones on the left side of the model, which change to grain-dominated packstones on the right side, cross flow does not occur in simulation EC-A (fig. 27). On the other hand, cross flow across parasequences 3 through 6 on the left side of the model is facilitated by the fact that the tight mudstone layers are discontinuous, whereas on the right side they are continuous (fig. 2). However, the spatial distribution of the higher-permeablity grainstone facies on the left part of the model in parasequences 1 and 2 (table 2, unit 10) and in parasequence 9 (table 2, unit 11) are crucial for cross flow through parasequences 3 through 6 on the left. As indicated in simulation EC-A (fig. 28), continuous mudstone layers do not necessarily represent flow barriers, as shown by the cross flow between parasequences 9 and 7 in the upper right of the model.

In the final simulation EC-F, the production well was located in the center of the model, and an injection well was placed at either side of the model. Prescribed pressures were adjusted in order to create the same pressure gradient between the

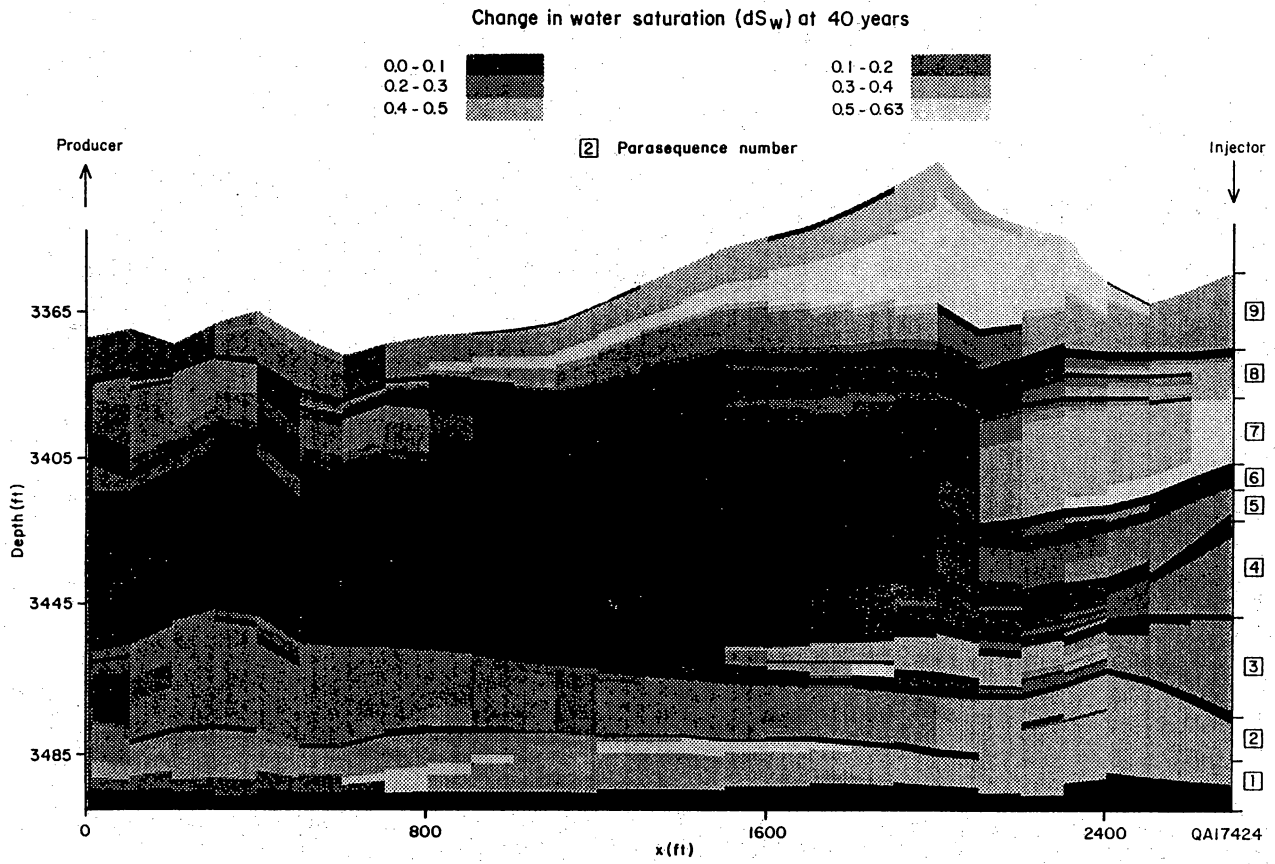

Figure 32. Computed changes in water saturation after 40 yr of waterflooding for simulation EC-R with inverse-injection pattern.

injection wells and production well as those used in the other simulations. As one would expect, initial production rates are much higher in simulation EC-F than those in the other simulations but subsequently show a much earlier and steeper decline. However, after 16,000 days, the production rate levels off at a slightly higher rate than that in simulation EC-A. Similar to the reverse-injection pattern in simulation EC-R, the water-cut curve breaks at a lower water-oil ratio than that in simulation EC-A (fig. 30). Simulation EC-I incorporates the flow pattern in the left part of the model similar to that in simulation EC-A, but on the right part of the model the flow behavior corresponds to that of simulation EC-R; consequently the sweep efficiency of simulation EC-F is lower than in simulation EC-A but slightly higher than in simulation EC-R (fig. 31).

VII. DISCUSSION

A. Implications of Outcrop Studies on Reservoir Characterization

Detailed geologic mapping of the upper San Andres Formation at the Lawyer Canyon area, Algerita Escarpment, yielded deterministic images of geologic facies architecture and corresponding porosity-permeability structure at scales ranging from a foot to tens of feet vertically and a foot to hundreds of feet laterally. The horizontal resolution of both the geologic facies mapping and the rock-property measurements allowed for detailed deterministic characterization of interwell heterogeneity. The geologic mapping within a sequence-stratigraphic framework calls for application to subsurface San Andres reservoirs in other parts of the Permian Basin, as well as to similar carbonate-ramp systems worldwide. A companion study is applying the general concepts derived from the outcrop study to the San Andres Seminole field, West Texas.

Geologic mapping revealed a series of upward-shallowing parasequences (10 to 40 ft thick and several thousand feet long). Parasequence boundaries are typically marked by tight mudstone/wackestone beds that display variable degrees of lateral continuity ranging from several hundred feet to more than 2,500 ft. Facies development within a parasequence can be highly variable. Generally, the thicker the parasequence, the more laterally variable is the resultant facies mosaic.

As documented by the flow simulations, the spatial distribution of permeable grainstone facies relative to the parasequence boundaries that show variable degrees of lateral continuity are crucial for understanding reservoir performance. Although it is difficult to extrapolate facies geometry in the interwell region in subsurface reservoirs, the outcrop study provides insight into the internal architecture of individual parasequences. Depositional processes in a ramp-crest environment produces upward-shallowing, upward-coarsening facies within a parasequence, starting with mudstone deposition associated with a rapid sea-level rise. Subsequently, carbonates are deposited as wackestone/packstone facies and finally as bar-crest and bar-flank grainstones and packstones. However, the lateral dimensions of these facies are highly variable and may not be penetrated by wells. The grainstone facies in parasequence 9 reaches a maximum thickness of 38 ft but quickly thins laterally and is completely absent at the northern and southern edges of the Lawyer Canyon parasequence window (fig. 2).

Within grainstones, permeability varies by as much as five orders of magnitude. Variogram analysis of spatial permeability in grainstone facies of parasequence 1 indicates short-range correlation but relatively high, locally random heterogeneity, reflected in a relatively high nugget compared with the sill. Similar permeability structures were obtained from the vuggy grainstone facies in parasequence 7. Flow simulations indicate that the effective permeability within the grainstone facies can be represented by the geometric-mean permeability. Note, however, that porosity-dependent capillary-pressure relationships, in combination with the small-scale heterogeneity, increase the sweep efficiency of individual facies. However, the effect is relatively small and will be outweighed by the sweep efficiency, which is largely controlled by injection practices and by the spatial distribution of individual facies relative to parasequence boundaries.

Reservoir-flow simulations of the entire outcrop model underscore the importance of knowing the facies architecture between wells. The simulation EC-DP, representing the standard approach for a subsurface reservoir model by linearly interpolating properties between wells, significantly overestimates the cumulative oil production compared with the base-case simulation EC-A, which incorporates the detailed spatial facies distribution between wells (fig. 31).

B. Determination of Remaining Oil

The changes in computed water saturation for simulation EC-A indicate that bypassing unswept oil through cross flow of injected water across low-permeability mudstones is an important mechanism. As a result, an area of unswept oil develops within parasequence 7 because of the slower advance of the water-injection front within parasequence 7. As shown in simulation EC-R, where the injection pattern is reversed, the cross-flow effect becomes more dominant and a greater area of unswept oil develops than in simulation EC-A. Comparison of production characteristics between simulation EC-A and EC-R indicates that simply changing the waterflood direction affects sweep efficiency. This implies that the spatial distribution of facies relative to the waterflood direction can significantly affect how the reservoir produces, as well as the volume and location of unswept oil.

The simulations further document that although the parasequence boundaries, represented by mudstone/wackestone units, strongly control waterflooding, these low-permeability mudstone layers do not necessarily represent flow barriers but can allow for significant cross flow. If, and when, cross flow occurs through these mudstones depends on the spatial distribution of the high-permeability grainstone facies relative to the waterflood direction.

Oil recovery in these simulations approaches 45 percent of total oil in place (fig. 31), which is high compared with oil-recovery data of San Andres reservoirs in the Permian Basin. However, the limitations of the two-dimensionality of the outcrop reservoir model overestimate sweep efficiency (Fogg and Lucia, 1990). The two-dimensionality of the cross-sectional model forces all fluid flow into the vertical plane between the wells and thus represents only the most direct flow between the injection and production wells. In three dimensions, flow away from the injection well and toward the production well is represented by radial streamlines characterized by increasing path length away from the most direct streamline between the wells. As a result, the water-breakthrough curves can be expected to be less steep in three-dimensional scenarios.

More important are the potential effects of three-dimensional heterogeneity, that is, possible circuitous flow paths perpendicular to the cross-sectional plane are not accounted for in the two-dimensional model. In addition to the effects of radial flow paths, neglecting heterogeneity in the third dimension also tends to overestimate sweep efficiency in the cross-sectional outcrop model. On the other hand, even less distinct mechanisms for trapping unswept oil indicated in the cross-sectional model may be enhanced when considering heterogeneity in the third dimension.

VII. SUMMARY

New approaches for reservoir characterization of heterogeneous carbonate-ramp deposits were presented that integrate geological, petrophysical, geostatistical, and reservoir-simulation studies of continuous outcrop of the San Andres Formation, New Mexico. Detailed geologic mapping revealed a series of upward-shallowing parasequences—10 to 40 ft thick and several thousand feet long—that form the geologic framework of the reservoir model. Parasequence boundaries, typically marked by tight mudstone/wackestone beds that display variable degrees of lateral continuity (ranging from several hundred feet to more than 2,500 ft) were shown to be important as potential flow barriers. To characterize the complex heterogeneity associated with depositional and diagenetic processes on the interwell scale, geologic and petrophysical data were collected from outcrops at the Lawyer Canyon area of the Algerita Escarpment. Detailed permeability measurements using both mini-air permeameter and core plugs were taken at different scales to characterize the spatial hierarchy of permeability patterns. Geostatistical analysis of permeability measurements indicated varying spatial correlation at different measurement scales. In all cases, however, permeability variability was characterized by substantial random heterogeneity at local scales.

Conditional simulations of permeability within individual facies showed apparent randomness owing to the large nugget effect. Waterflood simulations of conditional permeability realizations yielded results similar to those simulations using a geometric-mean permeability, indicating that the observed permeability heterogeneity within facies can be represented by a geometric mean. Mean permeabilities of most facies and rock fabrics differed significantly at the 95 percent confidence level and can be used to represent large-scale heterogeneity in reservoir-scale flow simulators.

Five basic rock-fabric units, identified in the Lawyer Canyon outcrop area, were incorporated into a geologic model describing the spatial distribution of depositional facies. Petrophysical parameters of these facies were derived on the basis of a petrophysical/rock-fabric approach using mean permeabilities, porosity, and saturation relationships characteristic of each rock fabric. Two-dimensional waterflood simulations were performed for the outcrop model to evaluate various factors affecting reservoir-flow behavior. The results indicated that the spatial distribution of high-permeability facies relative to the distribution of low-permeability parasequence boundaries, in conjunction with the waterflood direction, is crucial for predicting reservoir performance. The study also demonstrated that areas of unswept oil can result from cross flow across relatively low-permeability mudstone layers.

IX. REFERENCES

ECL Petroleum Technologies, 1990, ECLIPSE Reference Manual.

Ferris, M. A., in preparation, Permeability distribution on the upper San Andres Formation outcrop, Guadalupe Mountains, New Mexico: The University of Texas at Austin, Master's thesis.

Fogg, G. E., 1989, Stochastic analysis of aquifer interconnectedness: Wilcox Group, Trawick area, East Texas: The University of Texas at Austin, Bureau of Economic Geology Report of Investigations No. 189, 68 p.

Fogg, G. E., and Lucia, F. J., 1990, Reservoir modeling of restricted platform carbonates: Geologic/geostatistical characterization of interwell-scale reservoir heterogeneity, Dune field, Crane County, Texas: The University of Texas at Ausin, Bureau of Economic Geology Report of Investigations No. 190, 66 p.

Fogg, G. E., Lucia, F. J., and Senger, R. K., 1991, Stochastic simulation of interwell heterogeneity for improved prediction of sweep efficiency in a carbonate reservoir, *in* Lake, L. W., Carroll, H. B., Jr., and Wesson, T. C., eds., Reservoir Characterization II, San Diego, California: San Diego, California, Academic Press, p. 355–381.

Goggin, D. J., Thrasher, R. L., and Lake, L. W., 1988, A theoretical and experimental analysis of minipermeameter response including gas slippage and high velocity flow effects: In Situ, v. 12, no. 1/2, p. 79–116.

Hayes, P. T., 1964, Geology of the Guadalupe Mountains, New Mexico: U.S. Geological Survey Professional Paper 446, 69 p.

Hindrichs, S. L., Lucia, F. J., and Mathis, R. L., 1986, Permeability distribution and reservoir continuity in Permian San Andres shelf carbonates, Guadalupe Mountains, New Mexico, *in* Hydrocarbon Reservoir Studies — San Andres/ Grayburg Formations: Proceedings of the Permian Basin Research Conference, Permian Basin Section, Society of Economic Paleontologists and Mineralogists Publication No. 86-26, p. 31–36.

Honarpuour, Mehdi, Koederitz, L., and Harvey, H. A., 1982, Relative permeability of petroleum reservoirs: Boca Raton, Florida, CRC Press, 143 p.

Journel, A. G., and Huijbregts, Ch. J., 1978, Mining geostatistics: New York, Academic Press, 600 p.

King, P. B., 1948, Geology of the southern Guadalupe Mountains, Texas: U.S. Geological Survey Professional Paper 480, 183 p.

Kittridge, M. G., Lake, L. W., Lucia, F. J., and Fogg, G. E., 1990, Outcrop/subsurface comparisons of heterogeneity in the San Andres Formation: SPE Formation Evaluation, September 1990, p. 233–240.

Knudsen, H. P., and Kim, Y. C., 1978, A short course on geostatistical ore reserve estimation: University of Arizona, Department of Mining and Geological Engineering, 224 p.

Lucia, F. J., 1983, Petrophysical parameters estimated from visual descriptions of carbonate rocks: a field classification of carbonate pore space: Journal of Petroleum Technology, v. 35, no. 3, p. 629–637.

Radian Corporation, 1989, CPS-1 user's guide.

Warren, J. E., and Price, H. S., 1961, Flow in heterogeneous porous media: Society of Petroleum Engineers Journal, September 1961, p. 153–169.